



Power Electronic Systems
Laboratory

© 2022 IEEE

IEEE Journal of Emerging and Selected Topics in Power Electronics, Vol. 10, No. 4, pp. 4319-4335, August 2022

Geometrical Optimization of Medium-Frequency Air-Core Transformers for DCX Applications

T. Guillod,
P. Czyz,
J. W. Kolar

Personal use of this material is permitted. Permission from IEEE must be obtained for all other uses, in any current or future media, including reprinting/republishing this material for advertising or promotional purposes, creating new collective works, for resale or redistribution to servers or lists, or reuse of any copyrighted component of this work in other works



Eidgenössische Technische Hochschule Zürich
Swiss Federal Institute of Technology Zurich

Geometrical Optimization of Medium-Frequency Air-Core Transformers for DCX Applications

Thomas Guillod*, *Member, IEEE*,
Piotr Czyz*, *Student Member, IEEE*,
Johann W. Kolar*, *Fellow, IEEE*

*Power Electronic Systems Laboratory, ETH Zurich, Switzerland

Abstract—This paper analyzes the potential of air-core transformers (ACTs) for realizing medium-voltage high-power isolated DC-DC converters. ACTs, i.e., transformers without magnetic cores, are particularly interesting for their simple construction and reduced weight. However, the reduced magnetizing inductance, the reduced magnetic coupling, and the stray fields are challenging aspects for the design of ACTs. A comprehensive model of the ACT (e.g., magnetic field patterns, skin and proximity losses, shield's eddy currents, harmonics, insulation constraints, and thermal limit) is proposed and verified with measurements obtained with a prototype. Afterwards, a complete multi-objective optimization of a series resonant converter (SRC) operating as a DC transformer (DCX) between two 7kV buses with a rated power of 166kW is conducted. Two different geometries are considered for the ACT: concentric cylindrical coils and planar spiral coils. As a result, the optimal ACT, (operated at 162kHz) features extreme power densities of 7.5kW/dm³ and 31kW/kg, which confirms the superiority of ACTs regarding the gravimetric power density. The calculated efficiencies are 99.5% and 98.7% for the ACT and the complete DC-DC converter, respectively. Finally, the different trade-offs are highlighted and analyzed, e.g., mass, volume, efficiency, switching frequency, part-load behavior, and insulation distance.

Index Terms—DC-DC power converters, air-core transformer, power transformers, medium-frequency, medium-voltage, resonant converter, inductive power transmission, optimization methods, finite element analysis, lightweight converter.

I. INTRODUCTION

Isolated DC-DC converters are essential building blocks of modern high-power energy conversion systems, such as fast electric vehicle chargers, renewable energies, data-center power supplies, drive systems, or more electric aircraft [1]–[4]. The usage of medium-frequency transformers and wide-bandgap semiconductors allows the construction of more compact and efficient DC-DC converters [5]–[7]. Nevertheless, due to their limited gravimetric power density (i.e., 2–12kW/kg), the magnetic-core transformers (MCTs) are typically the heaviest components of power electronic systems. This is particularly problematic for airborne or battery-powered applications [2], [8]–[11].

In order to drastically reduce the weight of medium-frequency transformers, air-core transformers (ACTs), which consist of two coils that are magnetically coupled without the help of a magnetic circuit, have been proposed [10], [12], [13]. Even if air-core magnetic components are typically found in high-frequency low-power systems [14], [15], they are also interesting for high-power systems [13]. It has been

shown that ACTs can exhibit gravimetric power density above 25kW/kg with efficiencies above 99.5% [13]. Therefore, ACTs represent a promising alternative for weight-optimized converters with the following advantages:

- *Mass* - The magnetic core is typically the heaviest component of MCTs. Therefore, ACTs are significantly lighter than MCTs.
- *Linearity* - ACTs are perfectly linear and, therefore, can withstand significant temporary overcurrents or overvoltages without changing their properties.
- *Temperature* - The operating temperature of ACTs is not limited by the Curie temperature of the magnetic core. Therefore, ACTs are well suited for high-temperature environments.
- *Construction* - Due to their simple structure, ACTs facilitate the design of the mechanical parts and the cooling systems. Additionally, high-voltage electrical insulation can be easily integrated.
- *Electrical circuit* - The high leakage and low-magnetizing inductances of ACTs can be advantageous for some applications (e.g., LLC converter and resonant tank). Due to the possibility to integrate large insulation distances, ACTs also feature reduced parasitic capacitances.

However, removing the magnetic core has a critical impact on the magnetic field pattern of a transformer. This creates several challenges for the design and operation of ACTs:

- *Volume* - Without a magnetic core, the magnetic flux is not confined in the transformer. For this reason, ACTs are less compact than MCTs.
- *Electrical circuit* - The lower self-inductance and magnetic coupling of ACTs have to be considered for the converter design (i.e., increased magnetizing current, voltage drop under load).
- *Stray field* - The medium-frequency magnetic stray field emitted by ACTs is not negligible and should be shielded in order to avoid eddy current losses and/or electromagnetic interferences.
- *Modeling* - The magnetic field patterns of ACTs are difficult to approximate with accurate analytical equations. Moreover, the different parameters (e.g., voltage transfer ratio, leakage, and magnetizing) are difficult to decouple. This implies that numerical simulations and numerical optimization are typically required for ACTs.

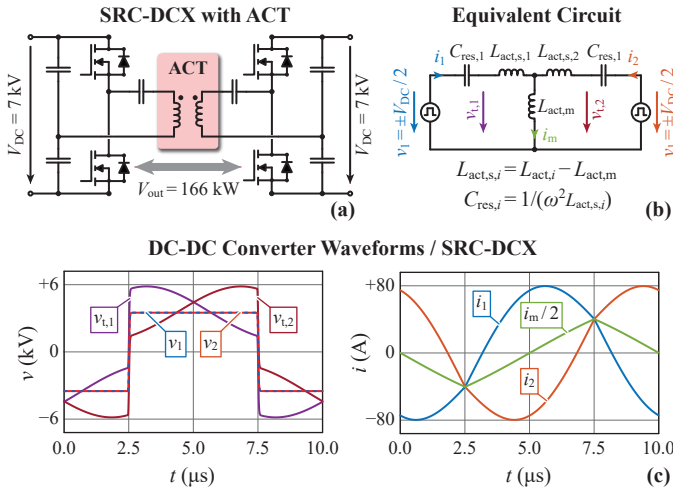


Fig. 1. (a) SRC-DCX DC-DC converter with an ACT. (b) SRC-DCX equivalent circuit using a T-shaped transformer circuit. (c) Voltage and current waveforms obtained with an active magnetizing current splitting SRC-DCX modulation ($P_{out} = 166$ kW, $V_{DC} = 7$ kV, $f = 100$ kHz, $L_{act,i} = 150$ μ H, and $L_{act,m} = 105$ μ H).

In many aspects, ACTs are similar to inductive power transfer (IPT) coils [16]–[19]. However, for ACTs, the air gap, which is only determined by the electric insulation distance, is much smaller and, therefore, the magnetic coupling is higher (i.e., 50–80%). Additionally, a misalignment between the coils can be excluded. These properties allow for the selection of a converter topology with a load-independent voltage gain, which is often desired for DC-DC converters. Several non-resonant (e.g., dual-active bridge) and resonant topologies (e.g., series-series and series-parallel) can be selected for systems with ACTs [4], [16].

In this paper, a series-series compensated system is selected for its simplicity, flexibility, quasi-sinusoidal currents, and ability to achieve zero voltage switching (ZVS) over the full load range. Fig. 1 shows the converter topology which corresponds to the well-known series-resonant converter (SRC) operated at the resonance frequency as a DC transformer (DCX) [5], [20], [21]. For the analysis, a 1 : 1 medium-voltage DC-DC converter operating between two 7 kV buses with a rated power of 166 kW is selected. Such systems are found in flexible bus-tie interconnection (current limit, power flow control, and fault handling) or in input-series output-parallel converter structures [4], [19]. However, the obtained results are also applicable to systems with arbitrary voltage transfer ratios.

The goal of this paper is to find and analyze the optimal coil geometry for ACTs [12], [13], [18]. Fig. 2 depicts the selected geometries: concentric cylindrical coils (C-ACT and DC-ACT) as used in [10], [13], planar spiral coils (S-ACT and DS-ACT) which are typically used for IPT systems [17], [18], and toroidal structures (T-ACT) [12]. In order to shield the ACT (magnetically and electrically), a conductive enclosure is placed around the coils [22]. All the parameters (e.g., wire size, coil size, insulation distance, placement of the shield, operating frequency, and semiconductor chip area) are optimized for the different geometries with an algorithm combining brute force grid search and genetic optimization [23], [24].

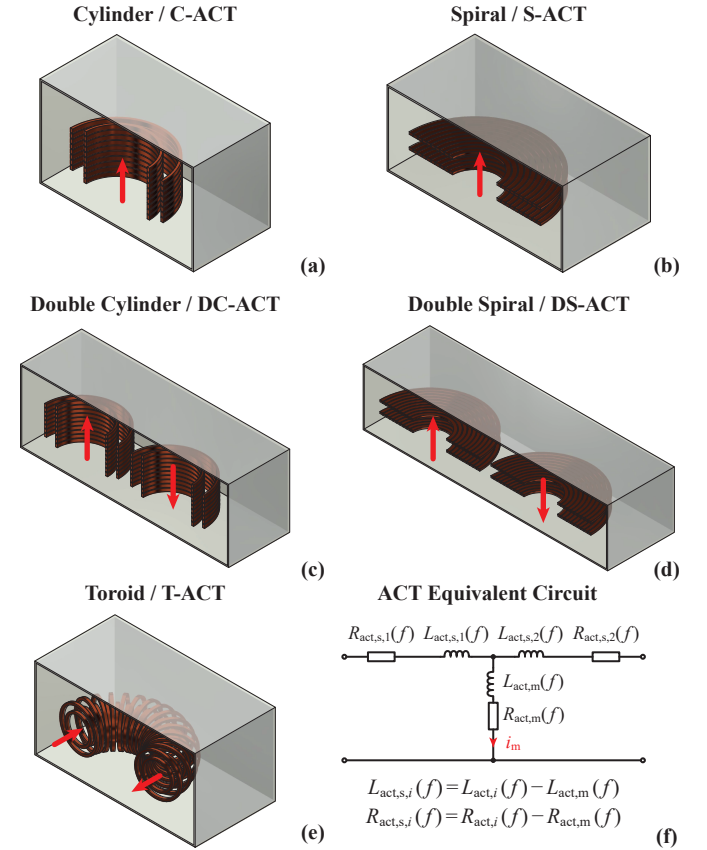


Fig. 2. (a) Cylindrical ACT (C-ACT). (b) Spiral ACT (S-ACT). (c) Double cylinder ACT (DC-ACT). (d) Double spiral ACT (DS-ACT). (e) Toroidal ACT (T-ACT). (f) Full ACT equivalent circuit (T-shaped). The ACT geometries are cut along a symmetry plane and half of the components are shown. The following color coding is used: sienna for the coils and gray for the conductive shield. The direction of the magnetic field produced by the magnetizing current (i_m) is highlighted in red.

This represents, to the knowledge of the authors, the first comprehensive modeling and analysis of ACTs with high magnetic coupling factors (i.e., magnetic field patterns, skin and proximity losses, shield's eddy currents, harmonics, insulation constraints, and thermal limit). This allows for a detailed characterization of the Pareto fronts and the underlying design trade-offs. Additionally, simple and general scaling laws, which describe the performance of ACTs, are proposed.

The paper is organized as follows. Section II introduces the ACT and SRC-DCX models. Section III provides experimental validation of the ACT model with the ACT prototype presented in [13]. Section IV describes the considered ACT and SRC-DCX design spaces and optimization strategies. The obtained Pareto fronts and optimal designs are discussed in Section V. Appendix A presents ACT scaling laws that allow the extrapolation of the presented results to different specifications. Finally, Appendix B describes the datasets and FEM models, which are available as supplementary material.

II. ACT AND SRC-DCX MODELS

In this Section, the working principle of the SRC-DCX with an ACT is explained and the models of the different

components (ACT, resonant capacitors, and semiconductor bridges) are detailed.

A. SRC-DCX Model

The SRC-DCX, cf. Fig. 1(a) is a LLC converter featuring a load-independent voltage transfer ratio without requiring close-loop control [20], [21]. The selected SRC-DCX features two MOSFET half-bridges with split DC-links as it reduces the number of switches and the voltage stress applied to the transformer [5]. Furthermore, the converter is bidirectional since both semiconductor bridges are constructed with active switches [5], [25].

In order to achieve a load-independent voltage transfer ratio, the transformer is operated at the resonance frequency, where the leakage impedance is compensated by the resonant capacitor impedance (cf. Fig. 1(b)). For the considered 1 : 1 voltage transfer ratio, the simple T-shaped equivalent circuit can be used and the resonant capacitors can be selected as

$$C_{\text{res},i} = \frac{1}{(2\pi f)^2 L_{\text{act},s,i}}, \quad (1)$$

where f is the operating frequency. Due to the resonance tank, a quasi-sinusoidal load current is flowing in the ACT (cf. Fig. 1(c)). It should be noted that the resonant tank can be located on the primary side, secondary side, or split between both sides [5], [16]. However, splitting the resonant capacitors between both sides is advantageous as it reduces the voltage stress applied to the ACT. Furthermore, for SRC-DCXs with arbitrary voltage transfer ratios, it is usually better to use a transformer equivalent circuit featuring an ideal transformer, as shown in [5], [26].

Besides the load current, a triangular magnetizing current is also flowing in the transformer and allows for ZVS of the MOSFETs. With the traditional SRC-DCX modulation scheme, the transmitter bridge is actively operated and the receiver bridge is operated as a passive or synchronous diode rectifier. Then, the magnetizing current is exclusively flowing on the transmitter coil and not on the receiver coil [21]. However, as shown in [5], the magnetizing current can be split between the coils if both bridges are actively switched with a small phase shift, cf. Fig. 1(c). Splitting the magnetizing current equalizes the switching speed of the MOSFETs and reduces the RMS currents. This is particularly important for ACTs, which feature low magnetizing inductances and high magnetizing currents.

The considered circuit model is fully coupled, i.e., all circuit equations are solved together without approximations. The complete magnetizing current splitting modulation scheme of SRC-DCX is considered with the following nonidealities: harmonic distortion, losses (ACT, resonant capacitors, and MOSFETs), frequency-dependency of the component values, and finite slew rate of the semiconductors (ZVS model).

B. Semiconductor and Resonant Capacitor Models

The semiconductor half-bridges are using SiC MOSFETs. The conduction resistance (R_{ds}) and the soft switching losses

(E_{sw}) are scaled with the chip area (A_{die}):

$$\begin{aligned} R_{\text{ds}} &= r_{\text{ds}}/A_{\text{die}}, \\ E_{\text{sw}} &= e_{\text{sw}}A_{\text{die}} + k_{\text{sw}}I_{\text{sw}}, \end{aligned} \quad (2)$$

where r_{ds} is the conduction resistance per chip area, e_{sw} the current-independent switching energy per chip area, k_{sw} the current dependency of the switching energy, and I_{sw} the switched current. The losses per chip area (h_{die}) are limited in order to ensure the thermal feasibility of the semiconductor half-bridges.

The resonant capacitors are realized with polypropylene film technology and the losses are modeled with a frequency-dependent dissipation factor ($\tan\delta$):

$$\tan\delta = \tan\delta_0 + k_\delta f, \quad (3)$$

where $\tan\delta_0$ is the frequency-independent dissipation factor, k_δ the frequency-dependency of the dissipation factor, and f the operating frequency.

The different coefficients representing the semiconductor (r_{ds} , e_{sw} , k_{sw} , and h_{die}) and resonant capacitor models ($\tan\delta_0$ and k_δ) can be approximated from the datasheets. However, for obtaining an accurate model, dedicated measurements are often preferable.

C. ACT Coil Geometries

Several geometries are suitable for the realization of ACTs, cf. Figs. 2(a)-(e). Due to the linearity of the ACT, all geometries feature the same, current-independent, equivalent circuit, cf. Fig. 2(f). Furthermore, these geometries can be classified into two categories:

- *Non-compensated field* - For the geometries shown in Figs. 2(a)-(b), the magnetic field generated by the magnetizing current is creating a stray field in the axis of the coils [10], [16].
- *Compensated field* - For the geometries shown in Figs. 2(c)-(e), the magnetic field generated by the magnetizing current is partially compensated, either with a double-D structure (two sets of coils) or with a toroidal structure [10], [12], [13], [18], [27]. This implies that the stray field is mostly confined inside the ACT.

The magnetic performance (coupling and stray field) of these configurations can be improved with the addition of magnetic cores, as often seen for IPT systems [17], [18], [27]. However, with magnetic cores, ACTs are losing their competitive advantage with respect to the gravimetric power density. Therefore, in this paper, no magnetic materials are used to guide the magnetic flux.

D. ACT Model

The ACT is composed of Litz wire windings surrounded by a conductive shield, which blocks the magnetic and electric stray fields (cf. Figs. 2(a)-(e)). In the windings, the skin depth should be larger than the strand diameter in order to mitigate the skin and proximity effects [28]. For the shield, the skin depth should be smaller than the wall thickness such that the magnetic field is blocked [28]. Due to the lack of accurate

analytical models for such configurations, the magnetic field patterns are simulated with a finite element method (FEM) in the frequency domain (2D or 3D models) [29]. In the FEM model, the discrete winding turns and the shield are modeled. The discrete strands of the Litz wire are, however, not considered for the FEM model in order to reduce the computational cost. This assumption can be done as the stranding of a perfectly twisted Litz wire does not impact the magnetic field pattern. The effect of the stranding of the Litz wire on the losses can be computed in the post-processing without degrading the accuracy of the results [28], [30].

Due to the frequency dependency of the eddy currents in the shield, static simulations cannot be used. Since the component is linear, the inductance and resistance matrices fully describe the ACT (cf. Fig. 2(f)). These matrices can be extracted from three linearly independent operating points:

$$\begin{aligned} \text{OP1: } \hat{i}_1 &= 1 \wedge \hat{i}_2 = 0, \\ \text{OP2: } \hat{i}_1 &= 0 \wedge \hat{i}_2 = 1, \\ \text{OP3: } \hat{i}_1 &= +1 \wedge \hat{i}_2 = -1. \end{aligned} \quad (4)$$

The inductance matrix is directly related to the energy stored in the magnetic field. The peak energy is extracted with the following integral:

$$\hat{W} = \iiint_{\text{all}} \frac{1}{2} \hat{B} \hat{H} dV. \quad (5)$$

From the peak energy obtained for the three linearly independent operating points, the inductance matrix can be easily computed as

$$\begin{aligned} L_{\text{act},1} &= 2\hat{W}_{\text{OP1}}, \\ L_{\text{act},2} &= 2\hat{W}_{\text{OP2}}, \\ L_{\text{act},m} &= \frac{1}{2} (L_{\text{act},1} + L_{\text{act},2}) - \hat{W}_{\text{OP3}}, \end{aligned} \quad (6)$$

where $\hat{W}_{\text{OP}i}$ represents the peak extracted energy (cf. (5)) for the operating point $\text{OP}i$ (cf. (4)). It should be noted that, the inductance matrix can also be extracted from the flux linkage between the coils or the induced voltages.

The extraction of the resistance matrix is more complex as it requires loss models for the Litz wire and the shield. From the FEM simulations, the following integrals are extracted:

$$\begin{aligned} \hat{K}_{J,\text{shield}} &= \iiint_{\text{shield}} \hat{j}^2 dV, \\ \hat{K}_{J,\text{winding},i} &= \iiint_{\text{winding},i} \hat{j}^2 dV, \\ \hat{K}_{H,\text{winding},i} &= \iiint_{\text{winding},i} \hat{H}^2 dV, \end{aligned} \quad (7)$$

where \hat{B} is the magnetic flux density, \hat{H} the magnetic field, \hat{j} the current density. The shield losses are generated by the eddy currents and can be expressed with the spatial integral of the current density, which leads to

$$P_{\text{shield}} = \frac{1}{2\sigma_{\text{shield}}} \hat{K}_{J,\text{shield}}, \quad (8)$$

where σ_{shield} is the electrical conductivity of the shield. For the Litz wire losses, the skin and proximity effects in the strands can be calculated as

$$\begin{aligned} P_{\text{winding,skin},i} &= \frac{F_r}{\sigma_{\text{winding}} k_{\text{winding}}} \hat{K}_{J,\text{winding},i}, \\ P_{\text{winding,prox},i} &= \frac{G_r k_{\text{winding}}}{\sigma_{\text{winding}} A_{\text{strand}}^2} \hat{K}_{H,\text{winding},i}, \end{aligned} \quad (9)$$

where σ_{winding} is the electrical conductivity of the strands, k_{winding} the Litz wire fill factor, and A_{strand} the cross section of a single strand. The factors F_r and G_r describe the skin and proximity effects in a single strand and are computed with Bessel functions, as shown in [28], [31], [32]. This model assumes a perfect twisting of the Litz wire, i.e., the current is equally shared between the strands [30]. From the computed losses (shield, skin effect, and proximity effect), the resistance matrix can be extracted as

$$\begin{aligned} R_{\text{act},1} &= 2P_{\text{OP1}}, \\ R_{\text{act},2} &= 2P_{\text{OP2}}, \\ R_{\text{act},m} &= \frac{1}{2} (R_{\text{act},1} + R_{\text{act},2}) - P_{\text{OP3}}, \end{aligned} \quad (10)$$

where $P_{\text{OP}i}$ represents the extracted losses (cf. (8) and (9)) for the operating point $\text{OP}i$ (cf. (4)). It should be noted that the resistance matrix can be computed for the complete ACT (total losses) or just for a sub-component (e.g., shield, primary winding, or secondary winding).

The electric field stress between the coils has two components: a common-mode voltage across the galvanic insulation and the differential-mode voltage across the coils. Under the assumption of a quasi-homogeneous field between the coils, the peak value of the electric field can be expressed as

$$\hat{E}_{\text{act}} = \frac{\hat{v}_{t,1} + \hat{v}_{t,2} + \hat{v}_{\text{CM}}}{d_{\text{iso}}}, \quad (11)$$

where $\hat{v}_{t,i}$ is the differential-mode voltage (cf. Fig. 1), \hat{v}_{CM} the common-mode voltage, and d_{iso} the insulation distance between the coils. For the electric field computation, the most critical case is considered, i.e., both differential mode voltages ($\hat{v}_{t,1}$ and $\hat{v}_{t,2}$) are added.

Due to the open structure of ACTs, an efficient forced air cooling of the coils is easily achievable [13]. More specifically, each coil can be cooled down from both sides. The thermal feasibility of the ACT is ensured by comparing the losses of the different components (primary coil, secondary coil, and shield) and the exposed area available for forced convection [13], [17].

E. Model Implementation

The aforementioned models allow for a fully coupled multi-objective optimization of the SRC-DCX [23], [33]. As shown in Fig. 3, the models are divided into two blocks, which are fully vectorized (parallel computing):

- *ACT FEM model* - The ACT FEM magnetic model is computed in the frequency domain for three linearly different operating points (cf. (4)). The figures of merit (cf. (5) and (7)) are extracted for a limited number

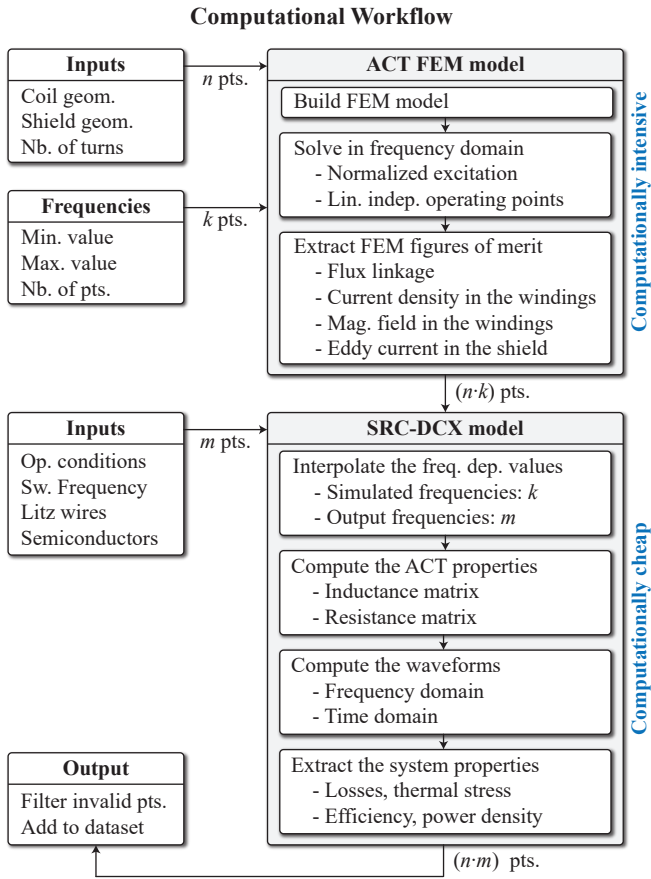
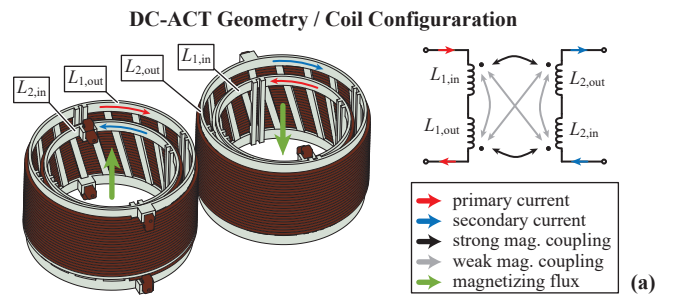


TABLE I
DC-ACT PROTOTYPE [13].

Specifications	
Topology	SRC-DCX with half-bridges
Power	166kW
DC bus	7kV / 7kV
ACT design	
Geometry	DC-ACT (cf. Fig. 2(c))
Frequency	77.4kHz
Coils	2×22 turns in series
Litz wire	$2000 \times 71\mu\text{m}$
Shield	0.5mm perforated aluminum
Fans	$4 \times 12\text{W}$
ACT performance	
Volume	$74.7\text{dm}^3 / 2.2\text{kW}/\text{dm}^3$
Mass	$10.1\text{kg} / 16.5\text{kW}/\text{kg}$
Losses	$0.85\text{kW} / 99.49\%$



Considered DC-ACT Prototype

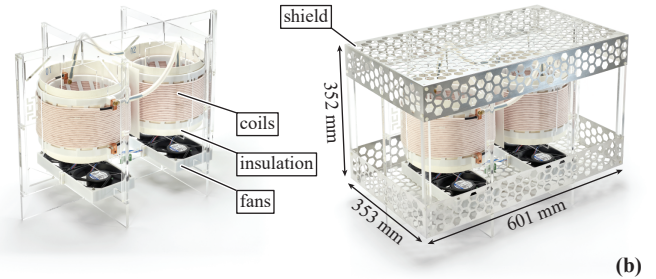


Fig. 3. Modeling workflow separating the computationally intensive ACT FEM models and the computationally cheap SRC-DCX model.

of frequencies in the range of interest. It has to be noted that all the properties computed in this step are independent of the operation condition (e.g., operating frequency, voltages, currents) of the ACT.

- *SRC-DCX model* - First, the FEM results are interpolated at the desired operating frequencies. The interpolation limits the number of required FEM simulations and is accurate since the extracted properties are only slightly frequency-dependent (cf. (5) and (7)). Afterwards, the frequency-dependent impedance matrices (cf. (6) and (10)), which include the high-frequency winding (skin and proximity effects) and shield (eddy-current) losses, are extracted. Finally, the SRC-DCX waveforms and the system properties (e.g., losses, efficiency, power density, and thermal limit) are computed.

The separation of the model into these two blocks allows for the isolation of the computationally intensive FEM task from the computationally cheap SRC-DCX model. Therefore, for each computed ACT geometry, many designs (e.g., operating frequency, Litz wire stranding, and chip area) can be extracted.

III. EXPERIMENTAL VALIDATION

The ACT model presented in Section II-D is compared with measurements obtained with the prototype presented in [13]. This ACT is part of a $P_{\text{out}} = 166\text{kW}$ SRC-DCX operating between two $V_{\text{DC}} = 7\text{kV}$ buses. The key parameters

Fig. 4. (a) DC-ACT geometry and equivalent circuit. (b) DC-ACT prototype (without and with the shield). A detailed description of the prototype can be found in [13].

are summarized in Tab. I. The prototype consists of two sets of coils connected in series (DC-ACT, cf. Fig. 2(c)) and is depicted in Fig. 4. Due to the magnetizing field compensation between the coil sets and the shield geometry (perforated shield above and below the coils), the prototype features a complex magnetic field pattern. Hence, this design is particularly interesting for validating the models. Extensive experimental validation of this prototype is presented in [13], including small-signal measurements, large-signal tests, resonance frequency analysis, thermal tests, and stray field measurements.

The comparison between small and large-signal measurements indicates that the ACT is perfectly linear. Therefore, the ACT terminal behavior is fully characterized by the impedance matrix. The impedance matrix, in turn, is fully identified from the open-circuit and short-circuit behaviors. Tab. II compares the measured and simulated values:

TABLE II
MEASURED AND SIMULATED PARAMETERS.

Var.	Meas.	Sim.	Err.
ACT inductances (without shield)			
Open circuit	214.4μH	203.9μH	4.9%
Short circuit	51.8μH	53.7μH	3.6%
ACT resistances (without shield)			
Open circuit	101.9mΩ	89.6mΩ	12.1%
Short circuit	151.9mΩ	118.6mΩ	21.9%
Shield impact on the inductances			
Open circuit	-3.7%	-3.4%	0.3%
Short circuit	-2.0%	-1.6%	0.4%
Shield impact on the resistances			
Open circuit	+57.3%	+52.6%	4.6%
Short circuit	+12.2%	+9.9%	2.2%

- *Inductances* - The ACT inductances are measured with a high precision impedance analyzer. The comparison between the measurements and the simulations indicates that the field pattern is correctly captured.
- *Resistances* - Due to the high quality factor of the ACT ($Q \approx 1000$ in open-circuit), electrical measurements of the winding resistance feature a limited accuracy. Therefore, highly accurate transient calorimetric measurements of the winding losses are performed [13]. The slightly increased resistances of the prototype are mainly explained by the imperfect twisting of the Litz wire, as shown in [13], [30].
- *Shield* - The impact of the shield on the inductances and resistances is assessed with a high precision impedance analyzer. The comparison between the measurements and the simulations demonstrates that the impact of the shield on the flux linkages and losses is correctly predicted.

Additionally, the measurements show that the self-resonance frequencies (open-circuit, short-circuit, and common-mode) are all located above 2MHz. This implies that the impact of the resonances and parasitic capacitances is negligible during nominal operation. Finally, the thermal capabilities of the ACT are inspected (for a maximum temperature elevation of 80°C). With the selected fans, 0.81kW of losses in the coils are achievable, leading to a dissipation per exposed area of 0.30W/cm². With the addition of air ducts, which improve the airflow around the coils, these numbers are increased to 1.28kW and 0.47W/cm².

IV. OPTIMIZATION BOUNDARY CONDITIONS

The considered SRC-DCX operates between two $V_{DC} = 7kV$ buses at a rated power of $P_{out} = 166kW$ (cf. Fig. 1), which are the same specifications as in [10], [13]. The maximum common-mode peak isolation voltage applied between the primary and secondary sides is $\hat{v}_{CM} = 14kV$. This Section describes the different parameters used in the optimization. Additionally, the multi-objective cost function and the optimization algorithm are described.

Even if the optimization is conducted with fixed specifications (166kW and 7kV), the obtained results are, to a

TABLE III
SEMICONDUCTOR AND RESONANT CAPACITORS / PARAMETERS.

Semiconductors	
$r_{ds} = 24.5\Omega mm^2$	Conduction resistance (at 125°C)
$e_{sw} = 2.04\mu J/mm^2$	Switching losses (current-indep.)
$k_{sw} = 3.03\mu J/A$	Switching losses (current-dep.)
$h_{die} = 2.00W/mm^2$	Maximum thermal dissipation
Resonant capacitors	
$\tan \delta_0 = 150ppm$	Dissipation factor (frequency-indep.)
$k_\delta = 2.5ppm/kHz$	Dissipation factor (frequency-dep.)

large extend, useful for other converter systems. In order to extrapolate the results, scaling laws are presented in Appendix A.

A. Semiconductor and Resonant Capacitor Model

Both half-bridges are realized with “Cree/Wolfspeed QPM3-10000-0300” 10kV SiC MOSFETs [34], [35]. The properties per chip area are considered and are depicted in Tab. III. The data are directly extracted from the calorimetric loss measurements shown in [36].

For the resonant capacitors, the properties of high-performance heavy-duty film capacitor “CELEM CSP 120/200” are taken [37]. The corresponding parameters are shown in Tab. III. The dissipation factor is measured with the calorimetric setup described in [38].

B. ACT Coil Geometries

The ACT geometries (non-compensated field, double-D, and toroidal structures) introduced in Section II-C feature distinct advantages and drawbacks, which can be summarized as follows:

- The non-compensated field structures (C-ACT and S-ACT, Figs. 2(a)-(b)) are magnetically advantageous (i.e., magnetic coupling, inductance, and quality factor). Due to the limited number of coils and structural elements, these geometries not only facilitate the cooling and the insulation design but also reduce the weight of the component [13]. However, these ACTs produce a significant magnetic stray field and, therefore, are potentially challenging to shield.
- Double-D structures (DC-ACT and DS-ACT, cf. Figs. 2(c)-(d)) allow for a reduction of the magnetic stray field. This leads to a reduction of the losses in the shield or, alternatively, the distance between the shield and the coils can be decreased [13]. However, splitting a large coil into two smaller coils is intrinsically not advantageous for the magnetic properties (i.e., magnetic coupling, inductance, and quality factor). This has a negative impact on the losses, volume, and mass of the component [18], [27].
- The toroidal structures (T-ACT, cf. Fig. 2(e)) are magnetically advantageous but suffer from practical issues concerning the thermal management, electrical insulation, coil former design, and winding realization. These drawbacks are particularly critical for a high-power

medium-voltage system; hence the toroidal geometries have been ruled out.

For the selected specifications, a preliminary Pareto analysis has shown that the double-D structures (DC-ACT and DS-ACT) are slightly inferior to the non-compensated field structures (C-ACT, and S-ACT). For a given power density (gravimetric or volumetric), the efficiencies of double-D designs are found to be 0.03 – 0.18% lower than the non-compensated field designs. It appears that, due to the high magnetic coupling factors achieved by ACTs (compared to IPT systems), the stray field produced by the non-compensated field structures can be shielded with moderate losses. Therefore, the reduction of the stray field achieved with double-D structures does not provide a sufficient advantage to compensate for their handicap with respect to the winding losses, mass, and volume. For these reasons, the non-compensated field geometries (C-ACT, and S-ACT, Figs. 2(a)-(b)) have been selected for a detailed analysis.

C. ACT Model

Besides the selection of the ACT coil geometry, several other design choices are required for the ACT. The selected parameters are shown in Tab. IV and explained as follows:

- *Winding* - Single-layer windings are used for the coils. Such windings are easier to construct, feature reduced stray capacitances, and do not require layer insulation.
- *Litz wire* - The coils are realized with profiled copper Litz wires. Aluminum Litz wires, which would be advantageous for the gravimetric power density, are not considered due to a lack of commercial availability. The size and aspect ratio of the Litz wire is limited in order to ensure manufacturability. A safety margin (10% for the skin effect losses and 30% for the proximity effect losses) is accepted for the winding losses, taking into account the impact of potential twisting imperfections. These safety margins are selected according to the measurements conducted in [13], [31] and the analysis presented in [30].
- *Shield* - The shield is made of non-perforated copper plates, which feature better performance than the perforated aluminum plates used in [13]. The thickness of the shield is selected with respect to the skin depth, ensuring the effectiveness of the shielding [13]. Openings in the shield are required for the cooling and the cable terminations and are causing eddy-current crowding in the shield. The impact of the openings has been assessed with FEM simulations and is found to increase shield losses by 20% to 30%. However, the optimization model does not consider the openings. Accordingly, a safety margin of 30% is added for the eddy-current losses.
- *Insulation* - An air insulation concept, which is compatible with medium-frequency electric fields with fast slew rates, is considered. As shown in [13], a dielectric barrier is placed between the coils in order to avoid a direct air clearance. The peak electric field between the coils is limited to a maximum value of 15kV/cm, which is below

the ionization electric field of air (ca. 25kV/cm) [39], [40]. Therefore, partial discharges, surface discharges, and problematic dielectric losses, which are particularly critical for converters with medium-voltage SiC devices, are not expected during rated conditions [41]–[43]. Besides being simple and robust, an air insulation concept also has the advantage to reduce the stray capacitances of the ACT.

- *Thermal management* - The ACT is cooled down with forced air cooling where the airflow is primarily directed towards the coils. The selected air insulation concept allows for a direct double-sided cooling of the coils and a conservative thermal limit of 0.28W/cm² is selected [13], [17]. The shield is cooled down by the residual airflow and a thermal limit of 0.15W/cm² is considered.
- *Construction* - The structural elements are constructed with glass-reinforced plastic, which brings high mechanical stability with reduced weight. The boxed volume of the ACT considers the coils, the shield, and the fans. The mass of the ACT consists of the coils, the shield, the coil formers, the electrical insulation, the structural elements, and the fans.

In order to reduce the computational effort, and due to the strong rotational symmetry of the selected geometries (C-ACT, and S-ACT), 2D axisymmetric FEM models are used for the optimization. The coils are fully rotational symmetric and can be modeled in 2D without any approximation. The rectangular cuboid shield is approximated by a cylinder with the same minimal distance between the shield and the coils. This approximation represents a conservative choice, which slightly overestimates the ACT losses (1% to 10%). At the end of the optimization process, the obtained designs are verified with 3D FEM models.

D. Optimized Input Variables

Fig. 5 shows the dimensions of the ACT, whereby all the parameters are optimized. The same Litz wire (dimension and number of strands) is used for both windings. It should be noted that, for ACTs, the voltage transfer ratio is not only proportional to the physical turn ratio but also depends on the geometry and position of the coils. For the C-ACT geometry, the inductance per turn differs for the primary and secondary windings, which feature different radii. Therefore, even for the selected 1 : 1 voltage transfer ratio, the C-ACT geometry requires a different number of turns for the primary and secondary windings. For the S-ACT, the same number of turns is used for both windings as both coils have the same dimension.

Furthermore, the Litz wire filling factor (k_{winding}) is optimized in order to find the optimal trade-offs between the weight, conduction losses, and proximity effect losses. The chip area per switch (A_{die}) is also swept as it represents a trade-off between conduction losses, switching losses, and cost. Finally, the operating frequency (f) is swept. All the optimized parameters are listed in Tab. V.

TABLE IV
ACT / PARAMETERS.

ACT Type	
Coils	C-ACT or S-ACT
Shield	Conductive shield
Litz Wire	
Type	Profiled Litz wire (rectangular)
Stranding	71 μm , less than 7'500 strands
Aspect ratio	Between 1:3 and 3:1
Skin effect losses	10% safety margin
Proximity effect losses	30% safety margin
Thermal limit	0.28W/cm ² for the exposed area
Op. temperature	130°C
Shield	
Type	Copper shield
Thickness	200% of the skin depth
Proximity effect losses	30% safety margin
Thermal limit	0.15W/cm ² for the exposed area
Op. temperature	70°C
Coil former and fans	
Peak electric field	Less than 15kV/cm
Coil former	Glass-reinforced plastic
Dielectric barrier	Nomex aramid polymer
Fan weight	1.0kg
Fan volume	2.0dm ³
Fan losses	70W

TABLE V
OPTIMIZED INPUT PARAMETERS.

ACT FEM model	
$n_{\text{turn},1} \in [5, 120]$	Primary number of turns (int.)
$n_{\text{turn},2} \in [5, 120]$	Secondary number of turns (int.)
$r_{\text{min}} \in [20, 180]$ mm	Minimum coil radius
$x_{\text{shield}} \in [20, 180]$ mm	Shield distance (x direction)
$y_{\text{shield}} \in [20, 180]$ mm	Shield distance (y direction)
$d_{\text{iso}} \in [5, 25]$ mm	Distance between the coils
$t_{\text{wire}} \in [0.5, 5.0]$ mm	Distance between the turns
$x_{\text{wire}}y_{\text{wire}} \in [6, 60]$ mm ²	Litz wire cross section
$x_{\text{wire}}/y_{\text{wire}} \in [1/3, 3]$	Litz wire aspect ratio
SRC-DCX model	
$k_{\text{winding}} \in [40, 48]$ %	Litz wire filling factor
$A_{\text{die}} \in [150, 300]$ mm ²	Chip area per switch
$f \in [25, 200]$ kHz	Operating frequency

TABLE VI
COMPUTED FIGURES OF MERIT.

ACT output variables		
V_{act}	dm ³	ACT boxed volume
m_{act}	kg	ACT mass
r_{act}	%	Ratio between the ACT height and width
$L_{\text{act},1}$	μH	ACT primary inductance
$L_{\text{act},2}$	μH	ACT secondary inductance
k_{act}	%	ACT magnetic coupling factor
C_{act}	pF	ACT interwinding capacitance
P_{act}	kW	ACT losses
\hat{E}_{act}	kV/cm	ACT peak electric field
h_{act}	W/cm ²	ACT thermal dissipation per area
ρ_{act}	kW/dm ³	ACT volumetric power density
γ_{act}	kW/kg	ACT gravimetric power density
η_{act}	%	ACT efficiency
SRC-DCX output variables		
A_{src}	mm ²	SRC-DCX total chip area
P_{src}	kW	SRC-DCX losses
κ_{src}	W/mm ²	SRC-DCX chip area power density
λ_{src}	%	SRC-DCX power factor
ξ_{src}	%	SRC-DCX peak voltage ratio
η_{src}	%	SRC-DCX efficiency

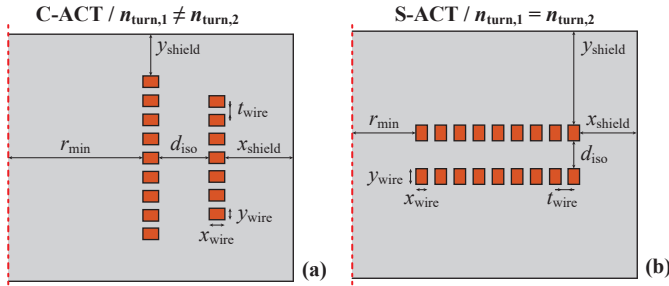


Fig. 5. (a) Geometry of the C-ACT. (b) Geometry of the S-ACT. The symmetry plane (3D model) or rotation axis (2D axisymmetric model) is indicated with a dotted red line.

E. Computed Output Variables

Tab. VI considers the figures of the merit of the ACT and SRC-DCX. Most of the listed parameters are typical for power electronic systems. However, three parameters are more specific to ACTs and are defined as (cf. Fig. 1)

$$\begin{aligned}
 k_{\text{act}} &= \frac{L_{\text{act},m}}{\sqrt{L_{\text{act},1}L_{\text{act},2}}}, \\
 \xi_{\text{src}} &= \max\left(\frac{\hat{v}_{t,1}}{V_{\text{DC}}/2}, \frac{\hat{v}_{t,2}}{V_{\text{DC}}/2}\right), \\
 \lambda_{\text{src}} &= \frac{P_{\text{out}}}{\frac{1}{2}\left(\frac{V_{\text{DC}}}{2}I_1 + \frac{V_{\text{DC}}}{2}I_2\right)},
 \end{aligned} \quad (12)$$

where k_{act} is the magnetic coupling of the ACT, ξ_{src} the ratio between the ACT peak voltage and the DC-link voltage, and λ_{src} the power factor between the transferred active power and the apparent power delivered by the semiconductor bridges. The following values would describe a SRC-DCX

with an ideal transformer [5]: $k_{\text{act}} = 100\%$, $\xi_{\text{src}} = 100\%$, and $\lambda_{\text{src}} = \sqrt{8}/\pi \approx 90\%$.

E. Design Space Exploration

The goal of the paper is to present a comprehensive view of the design space of ACTs. Therefore, the complete design space (cf. Tab. V) of the SRC-DCX has been systematically explored with a brute force strategy (using grid refinement for the Pareto optimal designs). In total, 2.0 million valid C-ACT geometries and 1.7 million valid S-ACT geometries have been simulated (ACT 2D FEM model, cf. Fig. 3). From the ACT FEM results, 127 million valid SRC-DCX designs are obtained (SRC-DCX model, cf. Fig. 3). The complete dataset is available as supplementary material, cf. Appendix B.

This dataset provides extremely interesting insight on the properties of ACTs with respect to the different performance metrics (e.g., volume, mass, chip area, efficiency, and magnetic coupling). However, the required computational

effort (6 days using two “AMD EPYC 7742” CPUs [44]) is unreasonable from a component design perspective.

G. Optimization Strategy

Fig. 6 depicts the optimization workflow used to design ACTs with a reasonable computation cost. More precisely, the optimal design is selected with respect to a multi-objective scalar cost function. The variables required for the ACT FEM model (cf. Tab. V) are optimized by a multi-objective genetic algorithm with the aim of efficiently exploring the design space [23], [24]. For the SRC-DCX model (cf. Tab. V), a brute force grid search approach can be used due to the reduced number of variables and the small computational cost. This hybrid optimization workflow, combining a genetic and brute force approach has two advantages: the number of FEM simulations is reduced (genetic algorithm) and the performed FEM simulations are fully exploited (brute force).

For the brute force grid search (SRC-DCX model), a regular grid with 3⁵000 points is considered. For the genetic algorithm (ACT FEM model), the following parameters are used [45], [46]:

- For the initialization step, 25⁴000 random combinations are considered. Using a large number of combinations ensures that designs with reasonable performance are present in the initialization pool.
- From the initialization pool, the 800 designs with the lowest cost function value are selected as the initial population of the genetic algorithm.
- After each iteration of the genetic algorithm, crossover and mutation are applied to the population with the following split: 50 elite children, 350 crossover children, 250 mutation children, and 150 random new combinations.
- The convergence of the genetic algorithm is evaluated over 10 generations with the following metrics: the relative change of the cost function (0.5% tolerance) and the relative change of the input (cf. Tab. V) and output (cf. Tab. VI) variables (3% tolerance).
- Convergence is typically reached after 120 generations, which implies that approximately 120⁴000 ACT geometries are simulated (including the initialization step). Given the number of optimized input variables (cf. Tab. V), this represents a massive improvement over brute force grid search. With two “AMD EPYC 7742” CPUs [44], the optimization is performed in 6 hours.

H. Multi-Objective Cost Function

The multi-objective cost function should be selected with respect to the constraints (e.g., target efficiency, target power density, production cost, and total cost of ownership) of the considered application (e.g., automotive, airborne, and stationary). As the ACT optimization presented in this work is not tied to a specific application, the cost function is selected to highlight the unique potential of ACTs to design power converters with extreme gravimetric power densities. A quadratic cost function is used and the weights

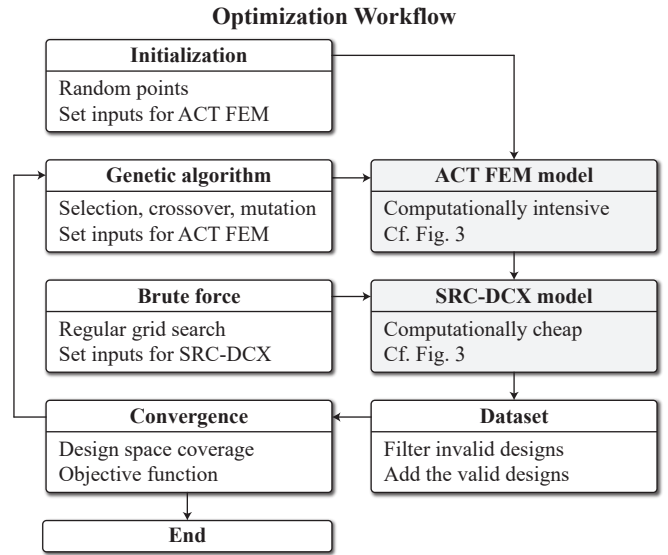


Fig. 6. Optimization workflow using a genetic algorithm for the ACT FEM model and brute force grid search for the SRC-DCX model.

(scaling factors) determine the desired trade-off between the objectives.

The selection of the weights typically requires several iterations. The initial weights are selected with respect to the desired performance. However, since the position and steepness of the Pareto optimal surface is, a priori, not known, the targeted performance might be exceeded or impossible to reach. In such cases, an adaptation of the weights is often required, using the dataset (initialization pool, population across the iterations, and optimal design) produced by the genetic algorithm with the previously selected weights.

In this paper, the cost function is decomposed into two parts. First, the ACT gravimetric power density, the ACT volumetric power density, and the SRC-DCX chip area power density (transferred power divided by the total installed semiconductor chip area) are considered. These three values are combined into a single power density cost function:

$$d = \sqrt{\frac{\left(\frac{8\text{kW/dm}^3}{\rho_{\text{act}}}\right)^2 + \left(\frac{30\text{kW/kg}}{\gamma_{\text{act}}}\right)^2 + \left(\frac{170\text{W/mm}^2}{\kappa_{\text{src}}}\right)^2}{3}}, \quad (13)$$

where the weights quantify the selected power density objectives. In order to highlight the potential of ACTs for realizing lightweight systems, the main weight (30kW/kg) is set for the gravimetric power density. The remaining weights (8kW/dm³ and 170W/mm²) are ensuring the competitiveness of ACTs with respect to typical values obtained with MCTs [10], [11].

In a second step, the obtained power density cost function (cf. (13)) is combined with the SRC-DCX losses (more precisely the loss fraction, 1 - η_{src}) in order to obtain the global multi-objective cost function:

$$c = \sqrt{\frac{d^2 + \left(\frac{1-\eta_{\text{src}}}{1.09\%}\right)^2}{2}}. \quad (14)$$

The weight on the loss fraction (1.09%) is iteratively selected such that, for the optimal design, the power density cost function approaches $d \approx 1$, i.e., the optimal design will meet the criteria defined in (13) with the highest possible efficiency.

V. OPTIMIZATION RESULTS

In this Section, the results obtained in Section IV are analyzed in detail. First, the Pareto fronts describing the performance space of the ACT and SRC-DCX are presented. Afterwards, the properties of the optimal design are discussed. Finally, the impact of the insulation requirement on the ACT is examined.

A. Pareto Fronts

The dataset described in Section IV-F is considered and Fig. 7 depicts the obtained Pareto fronts between the achieved efficiency (ACT and SRC-DCX) and power density (volumetric and gravimetric). The analysis of the Pareto fronts reveals the following characteristics:

- *Efficiency* - Despite the increased magnetizing current, high efficiency can be achieved for both the ACT (up to 99.65%) and the SRC-DCX (up to 99.05%).
- *Volume* - As already highlighted in [13], the $\eta_{act} - \rho_{act}$ Pareto front of ACTs is below what is achievable with MCTs. However, the optimization of the shield geometry presented in this work allows the achievement of volumetric power densities above $10\text{kW}/\text{dm}^3$, which is significantly higher than the results presented in [13].
- *Mass* - The main advantages of ACTs are their exceptional gravimetric power densities (up to $41\text{kW}/\text{kg}$, including the coil formers, the fans, the coils, and the shield), which is significantly higher than MCTs (typically below $12\text{kW}/\text{kg}$) [9]–[11]. This confirms that ACTs are particularly interesting for weight-constrained applications [2], [9].
- *Frequency* - The SRC-DCX can be operated in a large frequency range. Operation at high-frequency (above 100kHz) is still offering better performance, especially, for the gravimetric power density. Due to the low magnetizing inductance, ACTs are operated at higher frequencies than MCTs in order to limit the magnetizing current.

Fig. 8 shows the correlation between the SRC-DCX efficiency and the ACT gravimetric and volumetric densities. It can be seen that, for a given efficiency, interesting trade-offs exist between the gravimetric and volumetric densities.

B. Optimal Designs

The optimal designs (C-ACT and S-ACT) obtained with the aforementioned optimization workflow (cf. Section IV-G) and cost function (cf. Section IV-H) are depicted in Fig. 9. These optimal designs are computed with 3D FEM models and the deviation with respect to the 2D axisymmetric models is below 5% for all the considered variables (cf. Tab. VI).

Tab. VII and Tab. VIII describe the optimized input variables and the obtained figures of merit. Both ACT optimal

TABLE VII
OPTIMAL DESIGNS / PARAMETERS.

Var.	C-ACT	S-ACT
P_{out}	166 kW	166 kW
V_{DC}	7 kV	7 kV
\hat{v}_{CM}	14 kV	14 kV
$n_{turn,1}$	36	27
$n_{turn,2}$	29	27
r_{min}	64.0 mm	39.0 mm
x_{shield}	55.4 mm	35.9 mm
y_{shield}	44.5 mm	69.8 mm
d_{iso}	17.8 mm	18.0 mm
t_{wire}	1.3 mm	0.6 mm
x_{wire}	4.3 mm	3.4 mm
y_{wire}	3.3 mm	4.3 mm
$k_{winding}$	48.0%	48.0%
A_{die}	225.0mm^2	225.0mm^2
f	161.8 kHz	148.6 kHz

TABLE VIII
OPTIMAL DESIGNS / FIGURES OF MERIT.

Var.	C-ACT	S-ACT
V_{act}	22.3dm^3	24.2dm^3
m_{act}	5.2 kg	5.5 kg
r_{act}	81.8%	45.5%
$L_{act,1}$	89.6 μH	96.8 μH
$L_{act,2}$	83.7 μH	96.8 μH
k_{act}	63.1%	61.7%
C_{act}	49.6 pF	47.0 pF
P_{act}	0.89 kW	0.96 kW
\hat{E}_{act}	15.0 kV/cm	14.9 kV/cm
h_{act}	$0.28\text{W}/\text{cm}^2$	$0.28\text{W}/\text{cm}^2$
ρ_{act}	$7.5\text{kW}/\text{dm}^3$	$6.9\text{kW}/\text{dm}^3$
γ_{act}	$31.6\text{kW}/\text{kg}$	$29.9\text{kW}/\text{kg}$
η_{act}	99.46%	99.42%
A_{src}	900.0mm^2	900.0mm^2
P_{src}	2.19 kW	2.23 kW
κ_{src}	$184.4\text{W}/\text{mm}^2$	$184.4\text{W}/\text{mm}^2$
λ_{src}	79.2%	79.3%
ξ_{src}	187.4%	184.8%
η_{src}	98.68%	98.66%
c	1.11	1.14

designs feature extreme gravimetric power densities (above $25\text{kW}/\text{kg}$) while maintaining good efficiencies (above 99.4%) and volumetric power densities (above $6.5\text{kW}/\text{dm}^3$). The efficiencies of the complete optimal SRC-DCX systems are also above 98.6%.

Fig. 10 shows the magnetic field pattern without the shield. The magnetic field is mostly confined between the coils but a non-negligible stray field (above 5 mT) is also created by the magnetizing current. This issue is resolved by the conductive shield, as shown in Fig. 11. The eddy-currents in the shield are, as expected, completely blocking the magnetic field. It should be noted that, for the optimal designs, the shield is placed in the direct vicinity of the coil in order to limit the volume and the mass. This implies that the losses in the shield and the impact of the shield on the inductance matrix cannot be neglected. More specifically, the losses

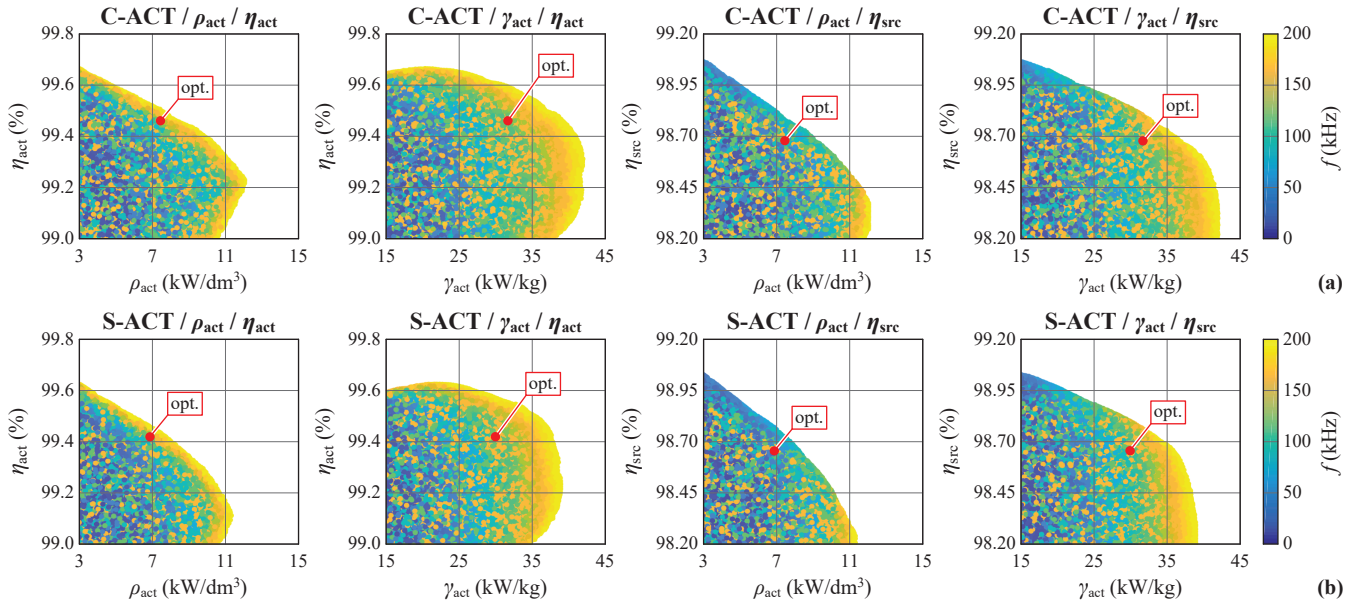


Fig. 7. Pareto fronts for (a) C-ACT and (b) S-ACT. The efficiency of the ACT and complete SRC-DCX are considered for both the gravimetric and volumetric densities. The frequencies (color map) are randomly sorted in order to show the design space diversity. The optimal designs (cf. (14)) are highlighted in red.

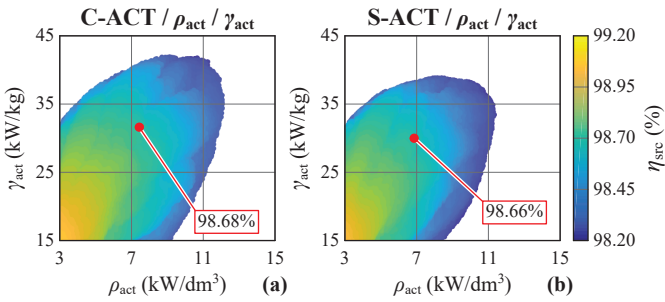


Fig. 8. Correlation between the gravimetric and volumetric densities for (a) C-ACT and (b) S-ACT. For each combination ($\rho_{act} - \gamma_{act}$), only the designs with the highest SRC-DCX efficiencies (color map) are shown. The optimal designs (cf. (14)) are highlighted in red.

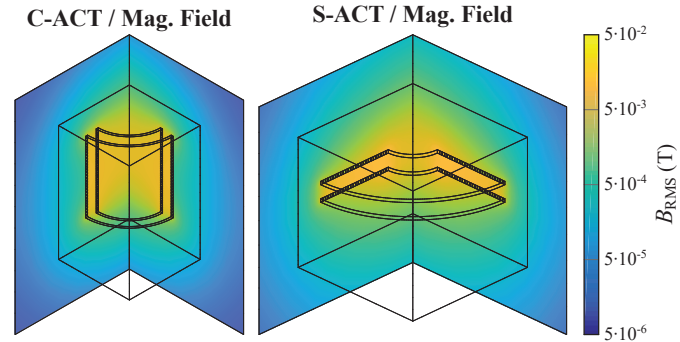


Fig. 10. RMS magnetic field produced by the ACT coils without shielding. As the ACT features symmetry planes, only one quarter of the geometry is shown. The position of the shield is indicated to allow for a direct comparison with Fig. 11.

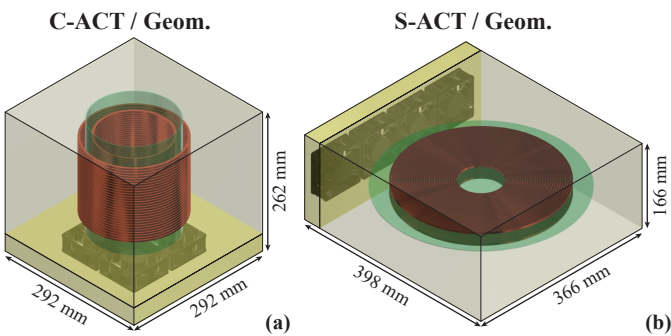


Fig. 9. (a) Optimal C-ACT geometry. (b) Optimal S-ACT geometry. The coils (sienna), the fans (yellow), the dielectric barrier (green), and the shield (gray) are depicted.

in the shield amount to 18% and 20% of the total C-ACT and S-ACT losses, respectively. However, these numbers could be reduced to 9% and 10% if the shield would be placed 20mm further away from the coils, indicating a clear trade-off between the shield losses and the power density.

C. Geometry Comparison

Fig. 7 reveals that the C-ACT and S-ACT feature extremely similar Pareto fronts. Nevertheless, the maximum volumetric and gravimetric power densities of the C-ACT designs are slightly superior: 7% and 6%, respectively. Fig. 8 shows that, for a given power density (gravimetric and volumetric), SRC-DCXs featuring C-ACTs are slightly more efficient (0.02 – 0.15%) than SRC-DCX with S-ACT.

A comparison between the optimal C-ACT and S-ACT designs (cf. Section V-B) also indicates a slight advantage for the C-ACT geometry with a 3% lower cost function value (cf. Section IV-H). However, all the parameters (e.g., frequency, inductance, volume, mass, and losses) are similar for both designs, indicating that the trade-offs are the same for C-ACT and S-ACT geometries.

It should be noted that, despite the lower performance, the S-ACT geometry has several advantages over the C-ACT. First, the S-ACT designs typically feature a flat geometrical

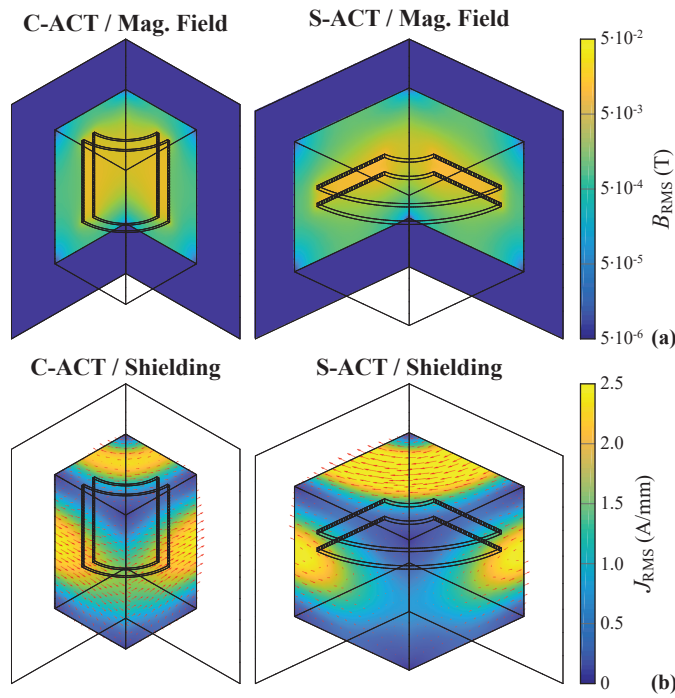


Fig. 11. (a) RMS magnetic field inside and outside the shield. (b) RMS eddy current density in the shield. As the ACT features symmetry planes, only one quarter of the geometry is shown.

aspect ratio, making them easier to integrate into converter systems. Additionally, the flat structure of S-ACT facilitates the coil former design, the cooling, and the common-mode insulation. Therefore, in many cases, the practical advantages of S-ACT compensate for the slightly increased losses.

Due to the similarities between the C-ACT and S-ACT geometries, the remaining analyses (loss sharing, part-load efficiency, frequency trade-off, design space diversity, and insulation distances) are conducted with C-ACT geometries. However, all the conclusions are also valid for S-ACT.

D. Volume, Mass, and Loss Sharing

Fig. 12 depicts the volume, mass, and loss sharing for the optimal C-ACT design (cf. Section V-B). It can be seen that the copper volume is almost negligible (less than 1%), explaining the reduced weight of the ACT. Most of the volume is the boxed volume around the coil and the boxed volume required for the shield. Therefore, it can be concluded that the volume of the ACT is only fully defined with a shield or a detailed stray field analysis. Due to the limited mass of the copper (coils and shield), the mass of the fans and structural elements is not negligible. Finally, even if the majority of the losses originates from the coils, the shield's eddy-current losses cannot be neglected either.

E. Part-Load Efficiency

The part-load behavior of a SRC-DCX using an ACT is of high interest. More particularly, the impact of large magnetizing currents and high operating frequencies (compared to systems using MCTs) should be examined. Fig. 13 shows the part-load behavior of the optimal C-ACT design (cf.

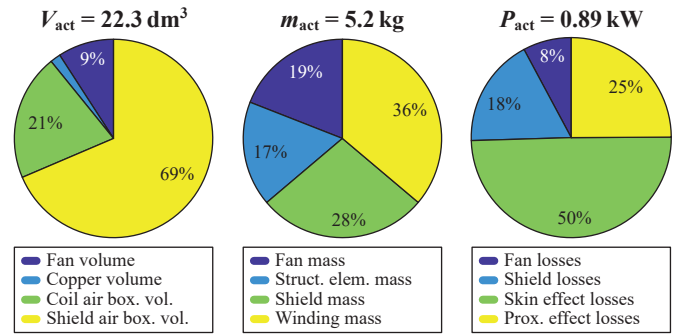


Fig. 12. Volume, mass, and loss sharing for the ACT. The optimal C-ACT design (cf. Section V-B) is considered.

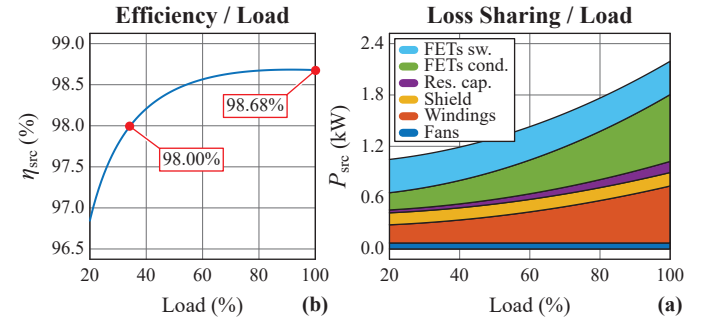


Fig. 13. (a) SRC-DCX efficiency. (b) Loss sharing. The optimal C-ACT design (cf. Section V-B) is selected and operated at different loads.

Section V-B). It can be seen that the SRC-DCX still features an efficiency of 98% at 33% load.

The part-load performance can be analyzed as follows. The MOSFET switching losses are load-independent. The winding losses, resonant capacitor losses, and the MOSFET conduction losses have two components: a quadratic term (proportional to the load current) and a constant term (due to the magnetizing current). Finally, the shielding losses are mostly load-independent, indicating they are mostly linked to the magnetizing current. It can be concluded that the part-load behavior of a SRC-DCX with an ACT is very similar to the case with a MCT. The impact of the magnetizing current losses in an ACT is comparable to the core losses in a MCT.

F. Optimal Operating Frequency

The choice of the operating frequency is one of the critical parameters for ACTs. In order to analyze the trade-offs, the optimal C-ACT design (cf. Section V-B) is selected and operated at different frequencies. All the other parameters (e.g., voltage, power level, and geometry) are kept constant, only the value of the resonant capacitors is adapted to the operating frequency. Fig. 14 shows the obtained results, which are interpreted as follows:

- **Power factor** - The impedance of the ACT is proportional to the frequency. This implies that the magnetizing current is inversely proportional to the frequency. Therefore, the power factor of the SRC-DCX (cf. (12)) increases with increasing frequency (towards the theoretical maximum of the SRC-DCX, $\sqrt{8}/\pi \approx 90\%$).
- **MOSFET switching losses** - As expected, the switching losses are increasing with the frequency. However,

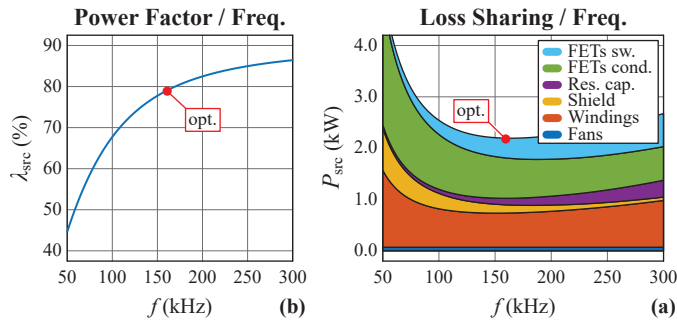


Fig. 14. (a) SRC-DCX power factor. (b) Loss sharing. The optimal C-ACT design (cf. Section V-B) is selected and operated at different frequencies. The optimal frequency is highlighted in red.

this effect is slightly mitigated by a reduction of the ZVS current, which is proportional to the magnetizing current (current-dependency of the ZVS losses, cf. (2)).

- *MOSFET conduction losses* - The conduction losses are quadratic with respect to the RMS current. Therefore, the conduction losses are reduced with increasing frequency (due to the increased power factor).
- *Resonant capacitor losses* - Two reasons explain the increase of the capacitor losses with the frequency: the frequency-dependency of the dissipation factor (cf. (3)) and the increased reactive power in the resonant capacitors.
- *Shield losses* - The fact that the shielding losses are decreasing with the frequency is astonishing. The resistance matrix describing the shield losses slightly increases with the frequency (approximately with the square root of the frequency). However, the eddy currents in the shield are mostly produced by the magnetizing current, which is inversely proportional to the frequency. As a result, the shield losses decrease with increasing frequency.
- *Winding losses* - The winding losses are quadratic with respect to the RMS current. The RMS current decreases with increasing frequency (due to the increased power factor). However, the resistance matrix describing the winding losses increases with the frequency (due to the skin and proximity effects). Therefore, with these two counteracting effects, the winding losses are optimal for a given frequency.

As shown in Fig. 14, the sum of all the loss components features a minimum at the optimal frequency. It should be noted that the optimal frequency of the ACT is, in the general case, different from the optimal frequency of the complete SRC-DCX. Furthermore, the optimum is flat with respect to the frequency, indicating that quasi-optimal losses are obtained for a wide range of frequencies.

G. Design Space Diversity

The aforementioned operating frequency trade-off indicates that the mapping between the design space (cf. Tab. V) and the performance space (cf. Tab. VI) is complex and very different designs will feature similar performance (i.e., design space diversity). Therefore, the design space diversity around

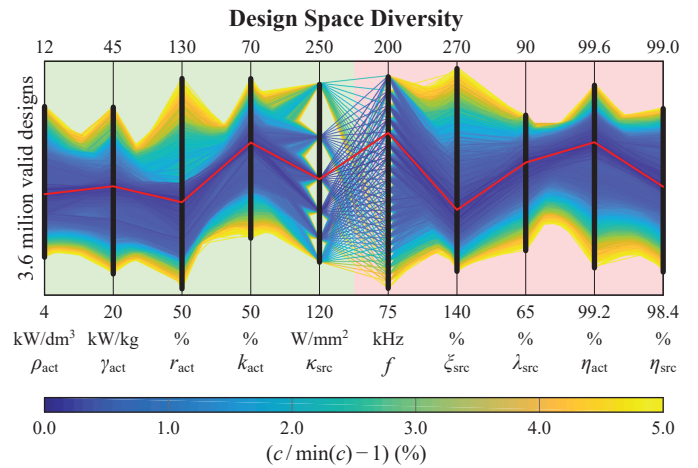


Fig. 15. Parallel coordinate plot of the quasi-optimal C-ACT designs. Each line represents a design with a cost function value close to the minima (within a 5% tolerance). In total 3.6 million quasi-optimal designs are plotted. The optimal C-ACT (cf. Section V-B) is highlighted in red.

the optimal C-ACT design (cf. Section V-B) is examined. All the designs with a cost function value (cf. Section IV-H) less than 5% above the minima are considered. Fig. 15 depicts all the obtained quasi-optimal designs in a parallel coordinate plot.

Many different designs are mapped to quasi-optimal cost function values. This implies that the optimum is flat and that many trade-offs exist. The design space diversity is particularly significant for the switching frequency considering that many effects compensate each other (cf. Fig. 14). It can also be seen that designs with the highest magnetic coupling and power factors are not automatically optimal since other factors are also important for the ACT (e.g., coil impedance, coil quality factor, and power density trade-offs).

Finally, the parallel coordinate plot is useful to select the proper cost function and to ensure that all the degrees of freedom in the design space have been leveraged. Due to the size of the design space and the complexity of the mapping between the design and performance spaces, a Pareto optimization with two variables (mass vs. losses or volume vs. losses) is not sufficient to capture the design trade-offs in a satisfactory manner. The parallel coordinate plot shows that multi-objective optimization (e.g., mass, volume, and efficiency) is required in order to extract the full potential of SRC-DCXs with ACTs.

H. Insulation Distance

As shown in Section V-A and Section V-B, high performance can be achieved with large insulation distances between the coils, allowing for an air insulation concept. However, a large insulation distance is diminishing the magnetic coupling of the ACT, leading to a reduced power factor (λ) and an increased peak voltage in the resonant capacitors (ξ). Therefore, examining the impact of the insulation distance on the system performance is interesting.

Fig. 16 depicts the obtained Pareto fronts (ACT and SRC-DCX) for different insulation distances (cf. (11)). The red curves show the Pareto fronts respecting the constraint

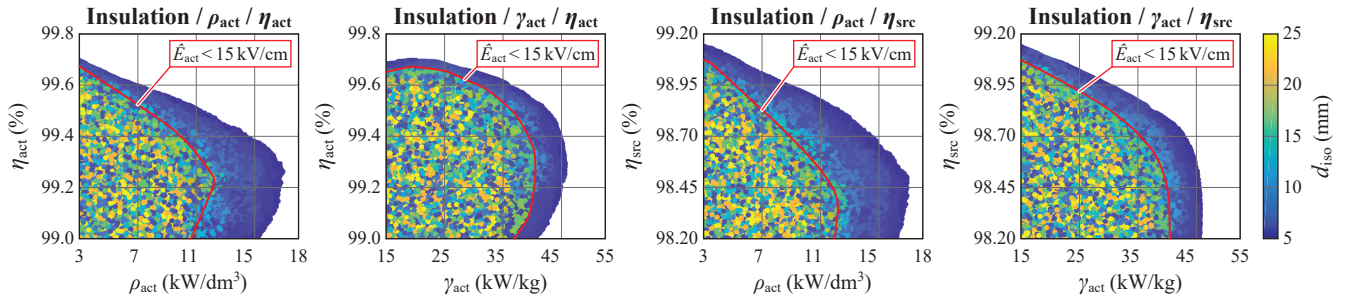


Fig. 16. Pareto fronts for different insulation distances (C-ACT geometries). The efficiency of the ACT and complete SRC-DCX are considered for both the gravimetric and volumetric densities. The insulation distances (color map) are randomly sorted in order to show the design space diversity. The red curves show the Pareto fronts respecting the constraint $\hat{E}_{act} < 15 \text{ kV/cm}$, which corresponds to the Pareto fronts shown in Fig. 7(a).

$\hat{E}_{act} < 15 \text{ kV/cm}$, which corresponds to the Pareto fronts shown in Fig. 7(a). As expected, designs with low insulation distances feature better performance, especially for the volumetric power density (i.e., 40% increase). However, the designs with low insulation distances would require dry-type or liquid insulation concepts which are significantly more complex (e.g., thermal management, partial discharges, dielectric losses, and manufacturing) [5], [41], [43]. These results also highlight that ACTs are an interesting concept for high-power low-voltage systems with reduced insulation requirements [12].

VI. CONCLUSION

This paper describes the modeling and optimization of an air-core transformer (ACT) for a medium-voltage DC-DC series resonant converter (SRC) operating as DC transformer (DCX) between two 7kV buses at a rated power of 166kW. Two different geometries are considered for the ACT, a structure with concentric cylindrical coils (C-ACT) and a flat structure with spiral coils (S-ACT). The ACT coils are realized with Litz wires and surrounded by a metallic shield that blocks the magnetic and electric stray fields.

A complete model of the SRC-DCX is presented with a special focus on the ACT. The ACT is modeled with FEM, taking into account the eddy currents in the shield, the skin and proximity losses, the impact of the harmonics, the thermal limit, and the insulation distances. The ACT model has been successfully validated with measurements. Due to the large number of variables, an optimization strategy that combines a genetic algorithm (for the ACT) and brute force grid search (for the SRC-DCX) has been implemented. This allows for the extraction of the multi-objective (volume, mass, chip area, and losses) optimal mapping between the design and performance spaces.

It has been shown that both geometries (C-ACT and S-ACT) are suitable for realizing ACTs and feature similar performance. The main advantage of ACTs is their gravimetric power density (up to 41 kW/kg), which is three to eight times higher than classical medium-frequency transformers. With the presented fully coupled model (co-optimization of the coils and the shield geometry), significant improvements of the volumetric power density of ACTs (up to 12kW/dm³) are obtained. Moreover, despite the limited magnetizing

inductance and magnetic coupling of ACTs, very good efficiencies are achievable for the complete SRC-DCX, i.e., up to 99.05%. Hence, it appears that ACTs are a competitive solution for DC-DC converters with weight constraints, high-temperature specifications, air insulation constraints, or strong linearity requirements.

Finally, the properties of the optimal systems are examined with respect to the loss sharing, the part-load behavior, the switching frequency, and the insulation distances. The ACTs are characterized by a very flat efficiency curve as well as flat loss optimum with respect to the operating frequency. However, it is found that the mapping between the design and performance space is complex, i.e., very different designs feature similar performances. This implies that numerical models and multi-objective optimization are required to fully exploit the great potential of ACTs.

APPENDIX

A. ACT Scaling Laws

The goal is to derive ACT scaling laws similar to the results obtained in [47] for MCTs. Scaling laws are not meant to provide accurate quantitative results but general qualitative statements about the performance achievable with ACTs for different power levels, power densities, and voltages. Hence, several assumptions are required in order to obtain closed-form solutions:

- *Circuit model* - The SRC-DCX depicted in Fig. 1, which features half-bridges with split DC-links and a 1 : 1 voltage transfer ratio, is considered. However, the extracted scaling laws are valid for any SRC-DCX configuration.
- *Waveform model* - A fundamental frequency approximation of the SRC-DCX waveforms, which include the load and magnetizing currents, is made.
- *Loss model* - The ACT winding losses, including the high-frequency effects, are considered. The losses produced by the semiconductors, the resonant capacitors, and the shield are neglected.
- *Winding model* - The windings are modeled as blocks, i.e., the discrete turns are not considered. The stranding (strand diameter and filling factor) is accepted to be constant. The number of turns is assumed to be

a continuous (non-discrete) variable and the same number of turns is used for both coils.

- *Scaling* - The volume of the ACT is scaled with a homothetic transformation, i.e., all the dimensions (e.g., Litz wire dimension, coil dimension, insulation distance, and shield geometry) are scaled together.

With these assumptions, the inductance and resistance matrices can be expressed as functions of the ACT box volume (V_{act}), the number of turns (n), and the operating frequency (f). The inductance matrix is frequency-independent and can be scaled as

$$L_{\text{act}}(V_{\text{act}}, n) = \begin{bmatrix} L_{\text{act},1} & L_{\text{act},m} \\ L_{\text{act},m} & L_{\text{act},2} \end{bmatrix} = V_{\text{act}}^{+\frac{1}{3}} n^2 L'_{\text{act}}, \quad (15)$$

where L'_{act} represents a scaled (per turn and per volume) inductance matrix. The frequency-independent resistance matrix (R_{lf}) is a diagonal matrix, which represents the low-frequency losses of the ACT windings [47]:

$$R_{\text{lf}}(V_{\text{act}}, n) = \begin{bmatrix} R_{\text{lf},1} & 0 \\ 0 & R_{\text{lf},2} \end{bmatrix} = V_{\text{act}}^{-\frac{1}{3}} n^2 R'_{\text{lf}}, \quad (16)$$

where R'_{lf} represents a scaled (per turn and per volume) low-frequency resistance matrix. The frequency-dependent resistance matrix (R_{hf}) contains off-diagonal elements and models the proximity effect losses of the ACT windings, which are quadratic with respect to the frequency [47]:

$$R_{\text{hf}}(V_{\text{act}}, f, n) = \begin{bmatrix} R_{\text{hf},1} & R_{\text{hf},m} \\ R_{\text{hf},m} & R_{\text{hf},2} \end{bmatrix} = V_{\text{act}}^{+\frac{1}{3}} f^2 n^2 R'_{\text{hf}}, \quad (17)$$

where R'_{hf} represents a scaled (per turn, per frequency, and per volume) high-frequency resistance matrix. Finally, the area available for the cooling of the coils can be expressed as a function of the boxed volume:

$$A_{\text{act}}(V_{\text{act}}) = V_{\text{act}}^{+\frac{2}{3}} A'_{\text{act}}. \quad (18)$$

The load and magnetizing current peak values can be computed with a fundamental frequency approximation, as shown in [5]. The following results are obtained:

$$\begin{aligned} \hat{i}_{\text{load}} &= \sqrt{2} \frac{\pi}{\sqrt{8}} \frac{P_{\text{out}}}{V_{\text{DC}}/2}, \\ \hat{i}_{\text{mag}} &= \frac{4}{\pi} \frac{V_{\text{DC}}/2}{2\pi f L_{\text{act},m}}, \end{aligned} \quad (19)$$

where P_{out} and V_{DC} represent the power flow and the DC-link voltage, cf. Fig. 1. It should be noted that the leakage impedances ($L_{\text{act},1} - L_{\text{act},m}$ and $L_{\text{act},2} - L_{\text{act},m}$) are canceled by the resonant capacitors and, therefore, have no impact on the load and magnetizing currents. The magnetizing current is equally split between the primary and secondary sides, leading to the following current phasors [5]:

$$\hat{i} = \begin{bmatrix} \hat{i}_1 \\ \hat{i}_2 \end{bmatrix} = \begin{bmatrix} +\hat{i}_{\text{load}} - j\frac{\hat{i}_{\text{mag}}}{2} \\ -\hat{i}_{\text{load}} - j\frac{\hat{i}_{\text{mag}}}{2} \end{bmatrix}. \quad (20)$$

With the defined resistance matrices (cf. (16) and (17)) and the current vector (cf. (20)), the main figures of merit of the ACT can be computed. More specifically, the ACT

losses, the loss fraction, the thermal stress, and the power density are extracted:

$$\begin{aligned} P_{\text{act}} &= \frac{1}{2} \hat{i}^* (R_{\text{lf}} + R_{\text{hf}}) \hat{i}, \\ \epsilon_{\text{act}} &= \frac{P_{\text{act}}}{P_{\text{out}}}, \\ h_{\text{act}} &= \frac{P_{\text{act}}}{A_{\text{act}}}, \\ \rho_{\text{act}} &= \frac{P_{\text{out}}}{V_{\text{act}}}. \end{aligned} \quad (21)$$

Additionally, the power factor of the SRC-DCX, which is a figure of merit for the reactive power delivered by the semiconductor bridges, is defined as

$$\lambda_{\text{src}} = \frac{P_{\text{out}}}{\frac{1}{2} \left(\frac{V_{\text{DC}}}{2} \frac{|\hat{i}_1|}{\sqrt{2}} + \frac{V_{\text{DC}}}{2} \frac{|\hat{i}_2|}{\sqrt{2}} \right)}. \quad (22)$$

The ACT losses are subject to the following trade-offs. Low operating frequencies and/or low numbers of turns are leading to large magnetizing currents (cf. (15) and (19)) and, therefore, large losses. On the other hand, high-frequencies and/or high numbers of turns are linked to large winding resistance matrices (cf. (16) and (17)). Therefore, the frequency and the number of turns feature an optimum:

$$(f_{\text{opt}}, n_{\text{opt}}) = \underset{f, n}{\text{argmin}} P_{\text{act}}(f, n). \quad (23)$$

Analytical expressions for f_{opt} and n_{opt} exist and can be easily extracted with a symbolic calculus tool. However, the obtained results cannot be written compactly and will not be presented in this work.

For the scaling laws, different boundary conditions are considered: constant volume, constant voltage, constant power, and constant power density. Additional, only optimal designs (cf. (23)) are used. The resulting scaling coefficients are depicted in Tab. IX and can be interpreted as follows:

- Changing the voltage level can be achieved by adapting the number of turns. All the other metrics (frequency, efficiency, thermal stress, and power factor) are not affected.
- A variation of the power level with a constant volume does not impact the operating frequency, the power factor, and the achieved efficiency. However, it should be noted that the maximum power level is limited by the thermal limit.
- Changing the ACT volume (homothetic transformation) with a constant power level does not impact the power factor. Large ACTs are more efficient and operated at lower frequencies. Compact designs will, under a certain volume, run over the thermal limit.
- The scaling of the power level with a constant power density indicates that high-power ACTs are more efficient and operated at lower frequencies. Nevertheless, the power factor and the thermal stress remain constant, indicating that ACTs are applicable for a wide range of power levels.

A comparison between Tab. IX and the MCT scaling laws presented in [47] reveals their similarities. Therefore, it can

TABLE IX
ACT SCALING LAWS ($f = f_{\text{opt}} \wedge n = n_{\text{opt}}$).

$V_{\text{DC}} = \text{var.} \wedge P_{\text{out}} = \text{const.} \wedge V_{\text{act}} = \text{const.}$		
f_{opt}	\propto	const.
n_{opt}	\propto	$(V_{\text{DC}})^{+1}$
ϵ_{act}	\propto	const.
h_{act}	\propto	const.
λ_{src}	\propto	const.
$P_{\text{out}} = \text{var.} \wedge V_{\text{act}} = \text{const.} \wedge V_{\text{DC}} = \text{const.}$		
f_{opt}	\propto	const.
n_{opt}	\propto	$(P_{\text{out}})^{-1/2}$
ϵ_{act}	\propto	const.
h_{act}	\propto	$(P_{\text{out}})^{+1}$
λ_{src}	\propto	const.
$V_{\text{act}} = \text{var.} \wedge P_{\text{out}} = \text{const.} \wedge V_{\text{DC}} = \text{const.}$		
f_{opt}	\propto	$(V_{\text{act}})^{-1/3}$
n_{opt}	\propto	const.
ϵ_{act}	\propto	$(V_{\text{act}})^{-1/3}$
h_{act}	\propto	$(V_{\text{act}})^{-1}$
λ_{src}	\propto	const.
$P_{\text{out}} = \text{var.} \wedge \rho_{\text{act}} = \text{const.} \wedge V_{\text{DC}} = \text{const.}$		
f_{opt}	\propto	$(P_{\text{out}})^{-1/3}$
n_{opt}	\propto	$(P_{\text{out}})^{-1/2}$
ϵ_{act}	\propto	$(P_{\text{out}})^{-1/3}$
h_{act}	\propto	const.
λ_{src}	\propto	const.

REFERENCES

- [1] A. Q. Huang, M. L. Crow, G. T. Heydt, J. P. Zheng, and S. J. Dale, "The Future Renewable Electric Energy Delivery and Management (FREEDM) System: The Energy Internet," *Proc. IEEE*, vol. 99, no. 1, pp. 133–148, 2011.
- [2] A. S. Gohardani, G. Doulgeris, and R. Singh, "Challenges of Future Aircraft Propulsion: A Review of Distributed Propulsion Technology and its Potential Application for the All Electric Commercial Aircraft," *Progress in Aerospace Sciences*, vol. 47, no. 5, pp. 369–391, 2011.
- [3] H. A. B. Siddique and R. W. De Doncker, "Evaluation of DC Collector-Grid Configurations for Large Photovoltaic Parks," *IEEE Trans. Power Del.*, vol. 33, no. 1, pp. 311–320, 2018.
- [4] J. W. Kolar and J. E. Huber, "Solid-State Transformers," in *Leistungselektronische Schaltungen: Funktion, Auslegung und Anwendung (in German)*, D. Schröder, Ed. Springer, Berlin Heidelberg, 2018.
- [5] T. Guillod, D. Rothmund, and J. W. Kolar, "Active Magnetizing Current Splitting ZVS Modulation of a 7kV/400V DC Transformer," *IEEE Trans. Power Electron.*, vol. 35, no. 2, pp. 1293–1305, 2020.
- [6] L. Wang, Q. Zhu, W. Yu, and A. Q. Huang, "A Medium-Voltage Medium-Frequency Isolated DC-DC Converter based on 15-kV SiC MOSFETs," *IEEE J. Emerg. Sel. Topics Power Electron.*, vol. 5, no. 1, pp. 100–109, 2017.
- [7] S. Zhao, Q. Li, F. C. Lee, and B. Li, "High-Frequency Transformer Design for Modular Power Conversion from Medium-Voltage AC to 400 VDC," *IEEE Trans. Power Electron.*, vol. 33, no. 9, pp. 7545–7557, 2018.
- [8] M. Mogorovic and D. Dujic, "100kW, 10kHz Medium Frequency Transformer Design Optimization and Experimental Verification," *IEEE Trans. Power Electron.*, vol. 34, no. 2, pp. 1696–1708, 2019.
- [9] C. Gammeter, F. Krismer, and J. W. Kolar, "Comprehensive Conceptualization, Design, and Experimental Verification of a Weight-Optimized All-SiC 2kV/700V DAB for an Airborne Wind Turbine," *IEEE J. Emerg. Sel. Topics Power Electron.*, vol. 4, no. 2, pp. 638–656, 2016.
- [10] P. Czyz, T. Guillod, F. Krismer, and J. W. Kolar, "Exploration of the Design and Performance Space of a High Frequency 166kW/10kV SiC Solid-State Air-Core Transformer," in *Proc. of the IEEE Energy Conversion Congr. and Expo. (ECCE Asia)*, May 2018.
- [11] P. Czyz, T. Guillod, F. Krismer, and J. W. Kolar, "Experimental Analysis of a 166kW Medium Voltage/Frequency Air Core Transformer for 1:1 DCX Applications," in *Special Session at the IEEE Energy Conversion Congr. and Expo. (ECCE USA)*, Oct. 2020.
- [12] V. Rigot, T. Phulpin, D. Sadarnac, and J. Sakly, "A New Design of an Air Core Transformer for Electric Vehicle On-Board Charger," in *Proc. of the European Conf. Power Electronics and Applications (EPE-ECCE Europe)*, Sep. 2020.
- [13] P. Czyz, T. Guillod, F. Krismer, J. Huber, and J. W. Kolar, "Design and Experimental Analysis of 166 kW Medium-Voltage Medium-Frequency Air-Core Transformer for 1:1-DCX Applications," *IEEE J. Emerg. Sel. Topics Power Electron. (early access)*, 2021.
- [14] Z. Zhang, K. Xu, Z. Xu, J. Xu *et al.*, "GaN VHF Converters With Integrated Air-Core Transformers," *IEEE Trans. Power Electron.*, vol. 34, no. 4, pp. 3504–3515, 2019.
- [15] S. Park and J. Rivas-Davila, "Isolated Resonant DC-DC Converters with a Loosely Coupled Transformer," in *Proc. of the Workshop on Control and Modeling for Power Electronics (COMPEL)*, Jul. 2017.
- [16] O. Knecht and J. W. Kolar, "Comparative Evaluation of IPT Resonant Circuit Topologies for Wireless Power Supplies of Implantable Mechanical Circulatory Support Systems," in *Proc. of the IEEE Applied Power Electronics Conf. and Expo. (APEC)*, Mar. 2017.
- [17] R. Bosshard and J. W. Kolar, "Multi-Objective Optimization of 50 kW/85 kHz IPT System for Public Transport," *IEEE J. Emerg. Sel. Topics Power Electron. (early access)*, vol. 4, no. 4, pp. 1370–1382, 2016.
- [18] J. Deng, W. Li, T. D. Nguyen, S. Li, and C. C. Mi, "Compact and Efficient Bipolar Coupler for Wireless Power Chargers: Design and Analysis," *IEEE Trans. Power Electron.*, vol. 30, no. 11, pp. 6130–6140, 2015.
- [19] H. Zhou, J. Chen, Q. Deng, F. Chen *et al.*, "Input-Series Output-Equivalent-Parallel Multi-Inverter System for High-Voltage and High-Power Wireless Power Transfer," *IEEE Trans. Power Electron.*, vol. 36, no. 1, pp. 228–238, 2021.
- [20] F. C. Schwarz, "A Method of Resonant Current Pulse Modulation for Power Converters," *IEEE Trans. Ind. Electron.*, vol. 17, no. 3, pp. 209–221, 1970.
- [21] V. Vorperian and S. Cuk, "A Complete DC Analysis of the Series Resonant Converter," in *Proc. of the IEEE Power Electronics Specialists Conf. (PESC)*, Apr. 1982.
- [22] *Guidelines for Limiting Exposure to Time-varying Electric and Magnetic Fields (1 Hz to 100 kHz)*, International Commission on Non-Ionizing Radiation Protection Std. ICNIRP, 2010.
- [23] A. Garcia-Bediaga, I. Villar, A. Rujas, L. Mir, and A. Rufer, "Multiobjective Optimization of Medium-Frequency Transformers for Isolated Soft-Switching Converters Using a Genetic Algorithm," *IEEE Trans. Power Electron.*, vol. 32, no. 4, pp. 2995–3006, 2017.

be concluded that ACTs represent an interesting alternative to MCTs for a large range of power levels, power densities, and voltages.

B. Datasets and FEM Models

The obtained results (cf. Section IV-F) for the SRC-DCX with C-ACT and S-ACT are available as supplementary material [48]. All the variables listed in Tab. VI and Tab. V are included for the 127 million valid designs. The datasets are proposed in two different formats: Python Pandas dataframe (saved as binary HDF5 file) and MATLAB table (saved as binary MAT file) [49]–[51].

The FEM models of the C-ACT and S-ACT are also available as supplementary material [48]. COMSOL is used as a FEM framework and the models are available as binary COMSOL MPH files, MATLAB files, and Java files [29]. The Litz wire coils and the conductive shield are modeled in the frequency domain. The following results are pre-defined and available in the simulation post-processing: the stored energy, the shield losses, and the Litz wire losses (skin and proximity effects).

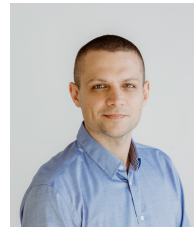
ACKNOWLEDGMENTS

The authors would like to thank Cindy Karina for the preliminary analysis of the C-ACT and S-ACT geometries. Additionally, the authors would like to show their gratitude to the high-performance computing group at ETH Zurich for providing the computational resources required for the presented analysis.

- [24] K. Watanabe, F. Campelo, Y. Iijima, K. Kawano *et al.*, "Optimization of Inductors Using Evolutionary Algorithms and its Experimental Validation," *IEEE Trans. Magn.*, vol. 46, no. 8, pp. 3393–3396, 2010.
- [25] J. Jung, H. Kim, M. Ryu, and J. Baek, "Design Methodology of Bidirectional CLLC Resonant Converter for High-Frequency Isolation of DC Distribution Systems," *IEEE Trans. Power Electron.*, vol. 28, no. 4, pp. 1741–1755, 2013.
- [26] T. Guillod, F. Krismer, and J. W. Kolar, "Magnetic Equivalent Circuit of MF Transformers: Modeling and Parameters Uncertainties," *Springer Electrical Engineering*, vol. 100, no. 4, pp. 2261–2275, 2018.
- [27] R. Bosshard, U. Iruretagoyena, and J. W. Kolar, "Comprehensive evaluation of rectangular and double-d coil geometry for 50 kw/85 khz ipt system," *IEEE J. Emerg. Sel. Topics Power Electron.*, vol. 4, no. 4, pp. 1406–1415, 2016.
- [28] J. A. Ferreira, *Electromagnetic Modelling of Power Electronic Converters*. Springer, Science & Business Media, 2013.
- [29] COMSOL, "COMSOL Multiphysics 5.4," Oct. 2018. [Online]. Available: https://doc.comsol.com/5.4/doc/com.comsol.help.comsol/COMSOL_ReferenceManual.pdf
- [30] T. Guillod, J. Huber, F. Krismer, and J. W. Kolar, "Litz Wire Losses: Effects of Twisting Imperfections," in *Proc. of the Workshop on Control and Modeling for Power Electronics (COMPEL)*, Jul. 2017.
- [31] M. Leibl, G. Ortiz, and J. W. Kolar, "Design and Experimental Analysis of a Medium Frequency Transformer for Solid-State Transformer Applications," *IEEE Trans. Emerg. Sel. Topics Power Electron.*, vol. 5, no. 1, pp. 110–123, 2017.
- [32] T. Guillod, "Litz Wire Losses with FEM and MATLAB," Aug. 2020. [Online]. Available: https://github.com/ethz-pes/litz_wire_losses_fem_matlab
- [33] R. M. Burkart and J. W. Kolar, "Comparative Life Cycle Cost Analysis of Si and SiC PV Converter Systems Based on Advanced η - ρ - σ Multiobjective Optimization Techniques," *IEEE Trans. Power Electron.*, vol. 32, no. 6, pp. 4344–4358, 2016.
- [34] J. B. Casady, V. Pala, D. J. Lichtenwalner, E. V. Brunt *et al.*, "New Generation 10kV SiC Power MOSFET and Diodes for Industrial Applications," in *Proc. of the Int. Exhib. and Conf. for Power Electronics, Intelligent Motion, Renewable Energy and Energy Management (PCIM Europe)*, May 2015.
- [35] Cree, "QPM3-10000-0300, Z-FET Silicon Carbide MOSFET," Oct. 2017.
- [36] D. Rothmund, D. Bortis, and J. W. Kolar, "Accurate Transient Calorimetric Measurement of Soft-Switching Losses of 10kV SiC MOSFETs and Diodes," *IEEE Trans. Power Electron.*, vol. 33, no. 6, pp. 5240–5250, 2018.
- [37] Celelem, "CSP 120/220, Conduction-Cooled Capacitor," Nov. 2019. [Online]. Available: https://www.celelem.com/Uploads/%D7%A8%D7%90%D7%A9%D7%99/csp%20120-200_spec.pdf
- [38] P. Papamanolis, T. Guillod, F. Krismer, and J. W. Kolar, "Minimum Loss Operation and Optimal Design of High-Frequency Inductors for Defined Core and Litz Wire," *IEEE Open Journal of Power Electronics*, vol. 1, pp. 469–487, 2020.
- [39] A. K uchler, *Hochspannungstechnik: Grundlagen – Technologie - Anwendungen (in German)*. Springer, Berlin, Heidelberg, 2009.
- [40] T. B. Gradinger, U. Drofenik, and S. Alvarez, "Novel Insulation Concept for a MV Dry-Cast Medium-Frequency Transformer," in *Proc. of the European Conf. Power Electronics and Applications (EPE-ECCE Europe)*, Sep. 2017.
- [41] K. Niayesh and E. Gockenbach, "On the Aging Mechanism of Solid Insulating Materials Exposed to Repetitive High Voltage Pulses," *IEEE Trans. Dielectr. Electr. Insul.*, vol. 21, no. 1, pp. 304–310, 2014.
- [42] *Safety Requirements for Power Electronic Converter Systems and Equipment - Part 2: Power Electronic Converters from 1 000 V AC or 1 500 V DC up to 36 kV AC or 54 kV DC*, IEC Std. 62477-2, 2018.
- [43] T. Guillod, R. F arber, F. Krismer, C. M. Franck, and J. W. Kolar, "Dielectric Losses in Dry-Type Insulation of Medium-Voltage Power Electronic Converters," *IEEE J. Emerg. Sel. Topics Power Electron.*, vol. 8, no. 3, pp. 2716–2732, 2020.
- [44] AMD, "AMD EPYC 7002 Series Processors," Apr. 2020. [Online]. Available: <https://www.amd.com/system/files/documents/AMD-EPYC-7002-Series-Datasheet.pdf>
- [45] D. A. Coley, *An Introduction to Genetic Algorithms for Scientists and Engineers*. World Scientific, 1999.
- [46] MathWorks, "Global Optimization Toolbox - User's Guide," Mar. 2021. [Online]. Available: https://www.mathworks.com/help/releases/R2021a/pdf_doc/gads/gads.pdf
- [47] T. Guillod and J. W. Kolar, "Medium-Frequency Transformer Scaling Laws: Derivation, Verification, and Critical Analysis," *CPSS Transactions on Power Electronics and Applications*, vol. 5, no. 1, pp. 18–33, 2020.
- [48] T. Guillod, "Air-Core Transformers for DCX Applications: Datasets and Models," Sep. 2021. [Online]. Available: <https://doi.org/10.3929/ethz-b-000520191>
- [49] Pandas Development Team, "Pandas: Powerful Python Data Analysis Toolkit, Release 1.3.2," Aug. 2021. [Online]. Available: <https://pandas.pydata.org/pandas-docs/version/1.3.2/pandas.pdf>
- [50] The HDF Group, "HDF5 User's Guide," Jun. 2019. [Online]. Available: https://portal.hdfgroup.org/download/attachments/53610087/Users_Guide.pdf
- [51] MATLAB, "MAT-File Format, R2021a," Mar. 2021. [Online]. Available: https://www.mathworks.com/help/releases/R2021a/pdf_doc/matlab/matfile_format.pdf



Thomas Guillod (M'18) received the M.Sc. and Ph.D. degree in electrical engineering from the Swiss Federal Institute of Technology (ETH) Zurich, Switzerland with a focus on power electronics, numerical analysis, and field theory, in 2013 and 2018, respectively. After a postdoc at the Power Electronic Systems Laboratory (ETH Zurich, Switzerland), he was working as an independent engineering consultant for both industrial and academic projects. In 2021, he joined that the Thayer School of Engineering at Dartmouth College, NH, USA as a research associate. His current research interests include high-frequency magnetic components, high-frequency power magnetic materials, and advanced numerical modeling techniques.



Piotr Czyz (S'14) received his B.Sc. and M.Sc. (summa cum laude) degrees in Electrical Engineering from the Gdansk University of Technology, in 2014 and 2015, respectively. In 2016 he was with C&T Elmech, Poland, working on the development of uninterruptible power supplies. In 2017 he began his Ph.D. at the Power Electronic Systems Laboratory (PES) at ETH Zurich and passed the doctoral examination in 2021. His research interests lie in the field of medium-voltage solid-state transformers technologies with the focus on medium-frequency transformers and power semiconductor stages.



Johann W. Kolar (M'89–F'10) received his M.Sc. and Ph.D. degree (summa cum laude) from the University of Technology Vienna, Austria, in 1997 and 1999, respectively. Since 1984, he has been working as independent researcher and international consultant in close collaboration with the Vienna University of Technology, in the fields of power electronics, industrial electronics and high performance drive systems. He was appointed Assoc. Professor and Head of the Power Electronic Systems Laboratory at the Swiss Federal Institute of Technology (ETH) Zurich on Feb. 1, 2001, and was promoted to the rank of Full Prof. in 2004. Dr. Kolar has proposed numerous novel converter concepts incl. the Vienna Rectifier, the Sparse Matrix Converter and the Swiss Rectifier, has spearheaded the development of x-million rpm electric motors, and has pioneered fully automated multi-objective power electronics design procedures. He has graduated 80 Ph.D. students, has published 900+ journal and conference papers and 4 book chapters, and has filed 200+ patents. He has presented 35+ educational seminars at leading international conferences and has served as IEEE PELS Distinguished Lecturer from 2012 – 2016. He has received 35+ IEEE Transactions and Conference Prize Paper Awards, the 2014 IEEE Power Electronics Society R. David Middlebrook Achievement Award, the 2016 IEEE PEMC Council Award, the 2016 IEEE William E. Newell Power Electronics Award, the 2020 EPE Outstanding Achievement Award and 2 ETH Zurich Golden Owl Awards for excellence in teaching. He was elected to the U.S. National Academy of Engineering as an international member in 2021. The focus of his current research is on ultra-compact/efficient WBG PFC rectifier and inverter systems, ultra-high BW switch-mode power amplifiers, multiport converters, Solid-State Transformers, multi-functional actuators, ultra-high speed/motor-integrated drives, bearingless motors, ANN-based multi-objective design optimization and sustainable systems.